RESEARCH ARTICLE

WILEY

In vivo disentanglement of diffusion frequency-dependence, tensor shape, and relaxation using multidimensional MRI

Jessica T. E. Johnson[1] | M. Okan Irfanoglu[2] | Eppu Manninen[1] |
Thomas J. Ross[3] | Yihong Yang[3] | Frederik B. Laun[4] | Jan Martin[5] |
Daniel Topgaard[5] | Dan Benjamini[1] (ORCID)

[1]Multiscale Imaging and Integrative Biophysics Unit, National Institute on Aging, NIH, Baltimore, Maryland, USA

[2]Quantitative Medical Imaging Section, National Institute of Biomedical Imaging and Bioengineering, National Institutes of Health, Bethesda, Maryland, USA

[3]Neuroimaging Research Branch, National Institute on Drug Abuse, National Institutes of Health, Baltimore, Maryland, USA

[4]Institute of Radiology, University Hospital Erlangen, Friedrich-Alexander-Universität Erlangen-Nürnberg (FAU), Erlangen, Germany

[5]Department of Chemistry, Lund University, Lund, Sweden

Correspondence
Dan Benjamini, Multiscale Imaging and Integrative Biophysics Unit, National Institute on Aging, NIH, Baltimore, MD, USA.
Email: dan.benjamini@nih.gov

Abstract

Diffusion MRI with free gradient waveforms, combined with simultaneous relaxation encoding, referred to as multidimensional MRI (MD-MRI), offers microstructural specificity in complex biological tissue. This approach delivers intravoxel information about the microstructure, local chemical composition, and importantly, how these properties are coupled within heterogeneous tissue containing multiple microenvironments. Recent theoretical advances incorporated diffusion time dependency and integrated MD-MRI with concepts from oscillating gradients. This framework probes the diffusion frequency, ω, in addition to the diffusion tensor, $\mathbf{D}$, and relaxation, R_1, R_2, correlations. A $\mathbf{D}(\omega) - R_1 - R_2$ clinical imaging protocol was then introduced, with limited brain coverage and $3\,\mathrm{mm}^3$ voxel size, which hinder brain segmentation and future cohort studies. In this study, we introduce an efficient, sparse in vivo MD-MRI acquisition protocol providing whole brain coverage at $2\,\mathrm{mm}^3$ voxel size. We demonstrate its feasibility and robustness using a well-defined phantom and repeated scans of five healthy individuals. Additionally, we test different denoising strategies to address the sparse nature of this protocol, and show that efficient MD-MRI encoding design demands a nuanced denoising approach. The MD-MRI framework provides rich information that allows resolving the diffusion frequency dependence into intravoxel components based on their $\mathbf{D}(\omega) - R_1 - R_2$ distribution, enabling the creation of microstructure-specific maps in the human brain. Our results encourage the broader adoption and use of this new imaging approach for characterizing healthy and pathological tissues.

KEYWORDS

denoising, diffusion tensor distribution, diffusion time dependency, diffusion-relaxation, human brain

1 | INTRODUCTION

Several MRI approaches are inherently sensitive to microstructural features on the order of micrometers, probing cell morphology and organization, though, currently, they contend with having poor spatial resolution. Notably, diffusion MRI (dMRI; Stejskal & Tanner, 1965) is an important tool that encodes diffusive water displacement, which is sensitive to cell membranes and physical barriers (Beaulieu, 2002; Leuze et al., 2017; Williamson et al., 2019), making it well-suited for indirectly assessing sizes and shapes of tissue components (Basser et al., 1994; Burcaw et al., 2015; Komlosh et al., 2018; LeBihan, 1990; Novikov et al., 2019; Pierpaoli et al., 1996). Relaxometry MRI is a complementary approach that encodes temporal magnetization decay (e.g., longitudinal and transverse relaxation rates, R_1 and R_2, respectively), which allows it to probe different water microenvironments and is especially sensitive to the local chemical composition, such as the presence and volume fraction of macromolecules (Bouhrara et al., 2020; Dvorak et al., 2021; Labadie et al., 2014; Mackay et al., 1994; Whittall & MacKay, 1989).

Emergent diffusion-relaxation multidimensional MRI (MD-MRI) acquisition protocols, combining the best elements of these approaches by encoding both diffusion and relaxation "dimensions" simultaneously (Hurlimann et al., 2006; Pizzolato et al., 2020; Stanisz & Henkelman, 1998), have become a focal point in the field. This imaging method introduces additional information, namely, the correlations between diffusivity and relaxation, invaluable to the study of tissue microstructure (Benjamini & Basser, 2017; Does & Gore, 2002; Kundu et al., 2023; Lundell et al., 2019; Peled et al., 1999; Veraart et al., 2018), brain connectivity (Benjamini & Basser, 2020; DeSantis et al., 2016; Slator et al., 2021), and pathology (Benjamini et al., 2021; Kim et al., 2017; Martin et al., 2021). Using diffusion acquisition schemes with free gradient waveforms (Sjolund et al., 2015) allows one to explore both the frequency-dependent and tensorial aspects of the encoding spectrum $\mathbf{b}(\omega)$ (Lasič et al., 2022; Lundell & Lasic, 2020), enabling the investigation of frequency/time-dependent changes of diffusion-relaxation correlations measures using a single framework (Narvaez et al., 2022). This approach provides nonparametric distributions of diffusion and relaxation components, and is based on the Gaussian phase distribution (GPD) approximation (Neuman, 1974; Stepišnik, 1981).

Recent major advances in clinical translation (de Almeida Martins et al., 2020; Reymbaut et al., 2021) led to an implementation of a $\mathbf{D} - R_1 - R_2$ imaging protocol on a clinical scanner comprised of 633 volumes in total, with varying diffusion weightings and directions, tensor ranks, echo times, and repetition times (Martin et al., 2021). However, despite its potential, this 25-min protocol did not provide full brain coverage (five axial slices) and had a relatively large $3\,\text{mm}^3$ voxel size. In addition, a proof-of-concept $\mathbf{D} - R_1 - R_2$ imaging protocol comprised of 134 volumes and 30 slices with $3\,\text{mm}^3$ voxel size was recently demonstrated (Yon et al., 2023). Nevertheless, whole brain coverage and higher spatial resolution are imperative for applications that requires identification and segmentation of brain regions,

thus enabling robust cohort studies. Therefore, designing a more efficient and sparse acquisition protocol is desirable.

In this study, we first present an efficient and sparse in vivo frequency dependent MD-MRI acquisition protocol that provides whole brain coverage at $2\,\text{mm}^3$ resolution. We demonstrate the feasibility and robustness of this pipeline using a well-defined phantom (Laun, Huff, & Stieltjes, 2009) and repeated scans of five healthy participants. Second, to explore noise effects in the data, we assert that while popular and effective denoising techniques, such as the Marchenko-Pastur PCA (MPPCA) method, exploit the inherent redundancy in dMRI data (Veraart, Fieremans, & Novikov, 2016), the sparse nature of the efficient MD-MRI encoding design cannot be considered highly redundant, and may require a more nuanced denoising strategy. Thus, we aimed to evaluate various denoising approaches and their impact on the reliability of outputs of the current MD-MRI framework. Analyzing the agreement between voxelwise $\mathbf{D}(\omega) - R_1 - R_2$ distributions across two scanning sessions in the human brain, we compactly quantify similarities across high-dimensional spectra between corresponding voxels using the Earth mover's distance (EMD; Rubner et al., 1998).

2 | MATERIALS AND METHODS

2.1 | Phantom

We used an anisotropic phantom (HQ imaging, Lörrach, Germany) to assess the robustness of our MD-MRI acquisition and processing pipeline, and the effects of different denoising strategies. The basic properties of this phantom have previously been described in detail (Laun, Huff, & Stieltjes, 2009). Briefly, the phantom consists of parallel polyamide fibers of 15 μm diameter wound on a circular polyoxymethylene spindle. An aqueous solution was used as embedded fluid between the fibers, resulting in restricted diffusion perpendicular to the fibers. The spindle with the fibers was immersed in an aqueous polyvinylpyrrolidone (PVP) solution (Pierpaoli et al., 2009; Wagner et al., 2017). This design creates two regions of interest (ROIs): fluid and tightly packed fibers, with isotropic and anisotropic diffusion characteristics, respectively.

2.2 | Participants

Five healthy participants (ages 41.2 ± 8.3, 3 women) were each scanned twice, a few weeks apart (i.e., total of 10 scans). Participants were systematically drawn from ongoing healthy cohorts of the National Institute on Drug Abuse (NIDA). Experimental procedures were performed in compliance with our local Institutional Review Board, and participants provided written informed consent. Prior to each scan, NIDA clinical and nursing units conducted Covid-19 testing, urine drug tests, a physical exam, and a questionnaire on pre-existing conditions and daily habits. Exclusion criteria included major

medical illness or current medication use, a history of neurological or psychiatric disorders or substance abuse.

2.3 | Data acquisition

Phantom and human data were acquired using a 3T scanner (MAGNETOM Prisma, Siemens Healthcare AG, Erlangen, Germany) with a 32 channel head coil. Data were acquired with 2 mm isotropic voxel size using a single-shot spin-echo echo planar imaging (EPI) sequence (Wetscherek et al., 2015) modified for tensor-valued diffusion encoding with free gradient waveforms (Martin et al., 2021). The acquisition parameters were set as follows: FOV = 228 × 228 × 110 mm^3, voxel size = 2 × 2 × 2 mm^3, acquisition bandwidth = 1512 Hz/Px, in-plane acceleration factor 2 using GRAPPA reconstruction with 24 reference lines, effective echo spacing of 0.8 ms, phase-partial Fourier factor of 0.75, and axial slice orientation.

The acquisition protocol was designed following previously described heuristic guidelines (Martin et al., 2021). A detailed summary of the acquisition protocol is displayed in Figure 1. In short, in addition to a $b = 0$ ms/µm^2 volume, numerically optimized (Sjolund et al., 2015) linear, planar, and spherical b-tensors were employed with b-values ranging between 0.1 and 3 ms/µm^2. Here we augment the data acquisition scheme with exploration of the ω-dimension of $\mathbf{b}(\omega)$ in the range of 6.6–21 Hz centroid frequencies, $\omega_{cent}/2\pi$, to allow the decoupling of frequency-dependent diffusion components.
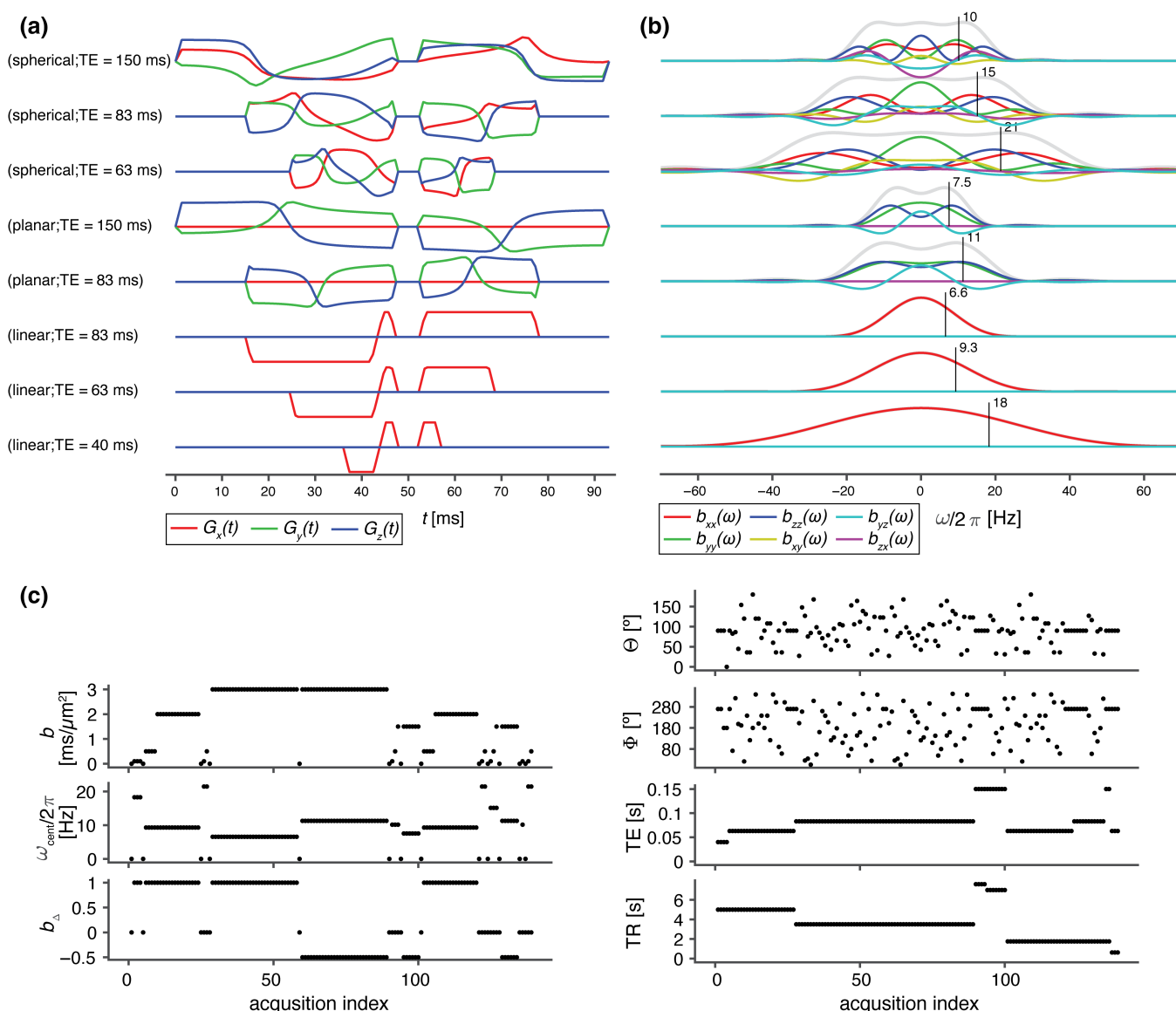

FIGURE 1 Key experimental details. (a) Time-dependent effective gradients $G(t)$ and (b) corresponding tensor-valued encoding spectra $\mathbf{b}(\omega)$ for linear, planar, and spherical encoding at different echo times and centroid frequencies, denoted by black vertical lines. (c) Acquisition protocol with repetition time TR, echo time TE, as well as **b**-tensor magnitude b, normalized anisotropy b_Δ (planar: -0.5, spherical: 0, linear: 1), orientation (Θ, Φ), and centroid frequency $\omega_{cent}/2\pi$, versus image acquisition index.

It should be noted that the highest frequencies reached for b-values of 0.5, 1.5, and 3 ms/μm^2 were 21, 15, and 11 Hz, respectively. The datasets were acquired with a single phase encoding direction (anterior to posterior, AP), and an additional $b = 0$ ms/μm^2 volume with reversed phase encoding direction (PA). Sensitivity to R_1 and R_2 was achieved by acquiring data with different combinations of repetition times, TR $= (0.62, 1.75, 3.5, 5, 7, 7.6)$ s and echo times, TE $= (40, 63, 83, 150)$ ms. The number of concatenations and preparation scans was increased to allow values of TR below 5 s.

The acquisition protocol we present here comprised of 139 individual measurements, with a scan time of $\sim$40 min. This protocol was designed by empirically selecting encoding parameters from the 633 $\mathbf{D} - R_1 - R_2$ imaging protocol (Martin et al., 2021) such that the signal differences between brain tissue types are maximized and signal to noise ratio (SNR) is preserved. In addition, the TE and (in particular) the TR ranges were extended to address shortcomings of the 633 volumes protocol. In our study, SNR, defined as the ratio between the $b = 0$ average signal intensity at the volume center, and the standard deviation of the signal intensity within a background region was 136 ± 14 for the in vivo data (averaged over all subjects and all repetitions), and 446 and 90 for isotropic and anisotropic regions of the phantom, respectively.

2.4 | Preprocessing and denoising strategies

Two denoising strategies were evaluated, in which MPPCA was applied on (1) the combined MD-MRI data and on (2) MD-MRI data grouped according to TE. These were compared with skipping the denoising step altogether and with a reference pipeline without any processing steps. The four strategies are schematically shown in Figure 2.

The preprocessing modules used in this work are part of the TOR-TOISE dMRI processing package (Irfanoglu et al., 2023; Pierpaoli et al., 2010). For the full pipeline, the dMRI data initially underwent denoising with the MPPCA technique (Veraart, Novikov, et al., 2016), which was followed by Gibbs ringing correction (Kellner et al., 2016) for partial k-space acquisitions (Lee, Novikov, & Fieremans, 2021). Motion and eddy currents distortions were subsequently corrected with TORTOISE's DIFFPREP module (Rohde et al., 2004) with a physically based parsimonious quadratic transformation model and a normalized mutual information metric. For susceptibility distortion correction, a T1W image was initially converted to a T2W image with $b = 0$ s/mm^2 contrast (Schilling et al., 2019), which was fed into the DRBUDDI (M. O. Irfanoglu et al., 2015) method for AP PA distortion correction. The final preprocessed data was output with a single interpolation in the space of an anatomical image at native in-plane voxel size. We note that the data did not contain any visible slice-to-volume motion or motion-induced signal dropouts, therefore, these options were disabled in the processing.

The extent of spatially correlated noise was quantified by computing the Global Moran Statistic (GMS), based on Local Indicators of Spatial Autocorrelation (Osadebey et al., 2019) for all volumes on our dataset from the background regions. Analyzing the GMS histograms, we did not observe a high level of spatial autocorrelation in our dataset.

We applied the original recommendation of choosing the patch size for MPPCA denoising so that the resulting matrices are
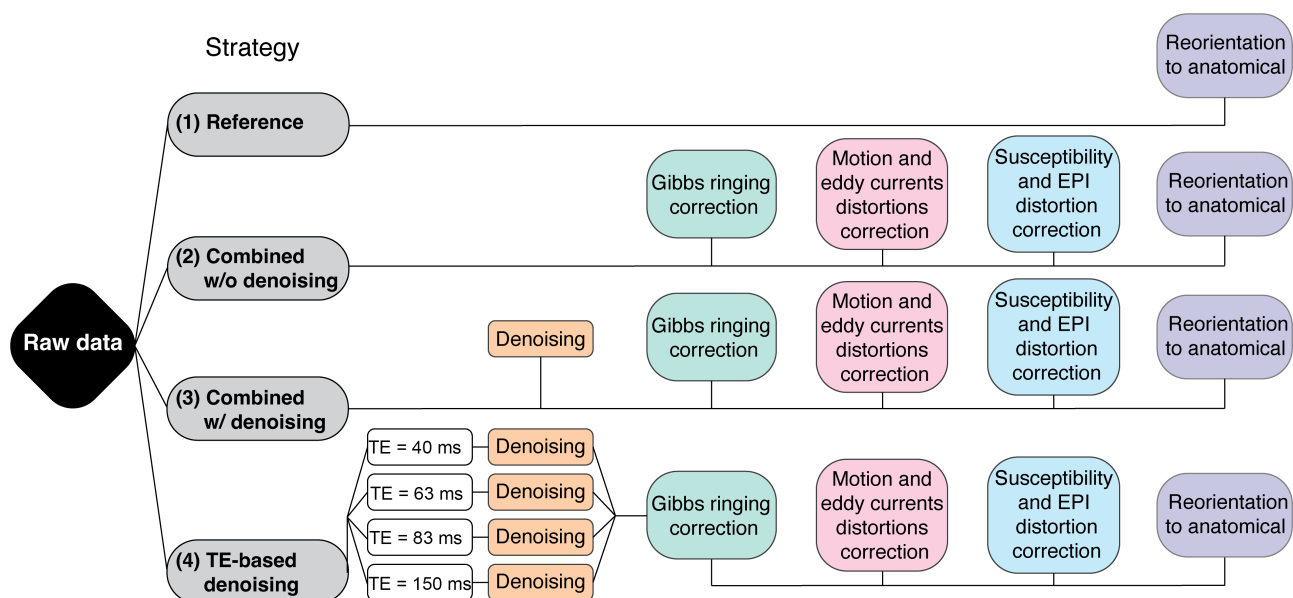

FIGURE 2 Schematic description of the evaluated denoising strategies. The Reference pipeline did not include any processing steps besides reorientation to the anatomical image space. In Strategies 2 and 3, all volumes, regardless of echo time/repetition time (TE/TR) and b-tensor encoding design, were initially combined into a single dataset. The MPPCA denoising step was skipped in Strategy 2, and turned on in Strategy 3. For Strategy 4, all datasets were grouped according to echo time prior to denoising. The grouped data were then combined again after denoising for the remainder of the pipeline.

approximately square (Veraart, Novikov, et al., 2016). When denoising the combined dataset, which consists of 139 volumes, the patch size was [5 × 5 × 5] voxels. When denoising data grouped according to TE (echo times of 40, 63, 83, 150 ms), which consists of 4, 49, 73, 13 volumes, respectively, the patch sizes were [2 × 2 × 2], [4 × 4 × 4], [4 × 4 × 4], and [2 × 2 × 2] voxels, respectively.

2.5 | Multidimensional data processing

The preprocessed data were processed in Matlab R2019b (MathWorks, Natick, MA) using the Monte Carlo inversion algorithm (Narvaez et al., 2022) as implemented in the multidimensional diffusion MRI toolbox (Nilsson et al., 2018). Briefly, the $\mathbf{b}(\omega) - \text{TE} - \text{TR}$ encoded signal S is modeled as a sum of contributions; the ith component is characterized by its signal weight, or fraction f_i, tensor-valued diffusion spectra $\mathbf{D}_i(\omega)$, and longitudinal and transverse relaxation rates $R_{1,i}$ and $R_{2,i}$ according to (Narvaez et al., 2022)

$$S[\mathbf{b}(\omega), \text{TE}, \text{TR}] = \sum_i f_i \exp\left(-\int_{-\infty}^{\infty} \mathbf{b}(\omega) : \mathbf{D}_i(\omega) d\omega\right) \\ [1 - \exp(-\text{TR}R_{1,i})] \exp(-\text{TE}R_{2,i}),$$

(1)

where the colon denotes a generalized scalar product.

As previously described in detail (Narvaez et al., 2021), inversion of Equation (1) is rendered tractable by approximating $\mathbf{D}_i(\omega)$ as axisymmetric Lorentzians parameterized by the zero-frequency axial and radial diffusivities $\left[D_{\|,i}, D_{\perp,i}\right]$, azimuthal and polar angles $[\Theta_i, \Phi_i]$, high-frequency isotropic diffusivity $D_{0,i}$, axial and radial transition frequencies, $\left[\Gamma_{\|,i}, \Gamma_{\perp,i}\right]$, along with longitudinal and transversal relaxation rates $[R_{1,i}, R_{2,i}]$. In this study, these parameters were sampled in the ranges $0.05 \leq D_{\|/\perp/0} \leq 5 \, \mu\text{m}^2/\text{ms}$, $0 \leq \Theta \leq \pi$, $0 \leq \Phi \leq 2\pi$, $0.2 \leq R_1 \leq 2 \, \text{s}^{-1}$, $1 \leq R_2 \leq 30 \, \text{s}^{-1}$, and $0.01 \leq \Gamma_{\|/\perp} \leq 10,000 \, \text{s}^{-1}$. The Monte Carlo inversion algorithm finds an ensemble of solutions within the above sampling range, and estimates the corresponding weights f via nonnegative least-squares, iterating this process while applying quasi-genetic filtering and bootstrapping with replacement to account for the inherent ill-conditioned nature of the Laplace inversion (Benjamini, 2020; de Almeida Martins & Topgaard, 2018). Following the terminology in (de Almeida Martins & Topgaard, 2018), the Monte Carlo inversion was performed with $N_{\text{in}} = 200$ input components, $N_p = 20$ proliferation steps, $N_m = 20$ mutation steps, up to 10 N_{out} output components, and $N_b = 100$ rounds of bootstrapping.

Voxelwise $\mathbf{D}(\omega) - R_1 - R_2$ distributions in the primary analysis space $\left[D_{\|}, D_{\perp}, \Theta, \Phi, D_0, \Gamma_{\|}, \Gamma_{\perp}, R_1, R_2\right]$ were evaluated at selected

values of ω within the narrow 6.6–21 Hz window actually probed by the gradient waveforms, giving a set of ω-dependent distributions in the $\left[D_{\|}(\omega), D_{\perp}(\omega), \Theta, \Phi, R_1, R_2\right]$ space. For each value of ω, the results are visualized as ω-independent distributions by projecting $D_{\|}(\omega)$ and $D_{\perp}(\omega)$ to the dimensions of isotropic diffusivity $D_{\text{iso}}(\omega)$ and squared normalized anisotropy $D_{\Delta}^2(\omega)$ (Conturo et al., 1996), according to

$$D_{\text{iso}}(\omega) = \frac{D_{\|}(\omega) + 2D_{\perp}(\omega)}{3},$$

(2)

and

$$D_{\Delta}^2(\omega) = \frac{\left(D_{\|}(\omega) - D_{\perp}(\omega)\right)^2}{\left(D_{\|}(\omega) + 2D_{\perp}(\omega)\right)^2}.$$

(3)

The means, variances, and covariances over relevant dimensions and subdivisions ("bins") of the distribution space are then computed. There are typically three bins in the in vivo human brain, roughly corresponding to white matter (WM), gray matter (GM), and CSF (Martin et al., 2021). These in vivo bins, which will be respectively referred to as bin 1, 2, and 3, represent partial integration regions in the $D_{\text{iso}} - D_{\Delta}^2$ distribution space, that is, bin 1: $D_{\text{iso}} < 2.5 \, \mu\text{m}^2/\text{ms}$ and $D_{\Delta}^2 > 0.25$; bin 2: $D_{\text{iso}} < 2.5 \, \mu\text{m}^2/\text{ms}$ and $D_{\Delta}^2 < 0.25$; and bin 3: $D_{\text{iso}} > 2.5 \, \mu\text{m}^2/\text{ms}$ and the full range of D_{Δ}^2. The normalized weights of these bins were mapped and are labeled as f_{bin1}, f_{bin2}, and f_{bin3}. The phantom we used has two distinct regions, isotropic and anisotropic diffusion, and therefore only two bins were used, with the following partial integration regions in the $D_{\Delta}^2 - D_{\text{iso}}$ distribution space: $D_{\text{iso}} < 1.25 \, \mu\text{m}^2/\text{ms}$ and $D_{\Delta}^2 > 0.40$ for bin 1 (anisotropic), and $D_{\text{iso}} > 1.15 \, \mu\text{m}^2/\text{ms}$ and $D_{\Delta}^2 < 0.12$ for bin 2 (isotropic). The normalized weights of these bins were mapped and are labeled as f_{aniso} and f_{iso}. Following conventions often used to display results from oscillating gradient encoding (Aggarwal et al., 2012) the effects of restricted diffusion were quantified by a finite difference approximation of the rate of change of the diffusivity metrics with frequency within the investigated window, which in our case was 21 and 6.6 Hz.

2.6 | Error estimates from phantom measurements

The ROIs from the isotropic and anisotropic portions of the phantom were used to assess the effect of different denoising strategies on the error estimate from the MD-MRI pipeline. We note that the signal intensity has been estimated from the fitted models; 100 bootstrap solutions have been estimated, the expected signal intensity for each measurement has been estimated from the models, and the median

over those signal estimates has been taken. Let $y_{m,v}$ be the measured normalized signal intensity of measurement (i.e., image volume) m at voxel v. Let $\widehat{y}_{m,v}$ be the estimated signal intensity.

We then compute the root mean square error (RMSE) for each measurement and for each voxel. To compute the RMSE for each measurement, $RMSE_m$, we square the difference between the measured and fitted voxel-wise normalized signal for each measurement and voxel, average those squared differences over the voxels and take the square root:

$$RMSE_m = \sqrt{\frac{\sum_{v=1}^{V}\left(y_{m,v}-\widehat{y}_{m,v}\right)^2}{V}}, \tag{4}$$

where V is the number of voxels.

To obtain the RMSE for each voxel, $RMSE_v$, (i.e., error for the whole fit instead of an error for each measurement), we compute

$$RMSE_v = \sqrt{\frac{\sum_{m=1}^{M}\left(y_{m,v}-\widehat{y}_{m,v}\right)^2}{M-N_v}}, \tag{5}$$

where $(M-N_v)$ is the error degrees of freedom, M is the number of measurements, and N_v is the number of estimated parameters at voxel v. The median value of N_v over the bootstraps is used because N_v can be different for each bootstrap.

2.7 | Variability analysis

The effect of different denoising strategies on the variability of the MD-MRI estimates was quantified by computing the distance between pairs of corresponding (i.e., voxelwise) $\mathbf{D}(\omega)-R_1-R_2$ distributions from the first and second scans within each participant. These computations were performed in the midway space between the scan and rescan volumes for each participant space using a rigid transformation to ensure that the image registration process exerted an equivalent influence on the scan and rescan data (Reuter et al., 2012; Veraart et al., 2021). This midway transformation was applied to the discrete $\mathbf{D}(\omega)-R_1-R_2$ coordinates $\left[D_{\parallel}(\omega),D_{\perp}(\omega),\Theta,\Phi,R_1,R_2\right]$ and their respective weights in each imaging session's native space, bringing each map to the midway point between the scan and rescan sessions.

We propose here the EMD (Rubner et al., 1998) as a novel distance measure between $\mathbf{D}(\omega)-R_1-R_2$ distributions, once both scan sessions have been transformed to the midway space. In the current context, the EMD between voxelwise distributions obtained from two scans from the same subject will produce a complete description of the variability using different denoising strategies. The EMD computes the distance between two distributions of any dimension, expressed as discrete coordinates and weights (as in the current

implementation), or as density functions (continuous representations, e.g., Benjamini et al., 2020), which are represented by signatures. The signatures are sets of weighted features that capture the distributions. In our case, the features were the discrete $\mathbf{D}(\omega)-R_1-R_2$ coordinates $\left[D_{\parallel}(\omega),D_{\perp}(\omega),\Theta,\Phi,R_1,R_2\right]$.

As described in Section 2.5, each voxel contains $N_b = 100$ bootstrap estimates of $\mathbf{D}(\omega)-R_1-R_2$. Therefore, all discrete coordinates within each bootstrap iteration, $\left[D_{\parallel}(\omega),D_{\perp}(\omega),\Theta,\Phi,R_1,R_2\right]_n$, and their respective weights, f_n, were joined together, followed by a final normalization step of the weights. The EMD is defined as the minimum amount of "work" needed to change one signature into the other. The work is based on predefined ground distance, that is, the distance between two features in corresponding voxels, which was chosen here to be Euclidean distance. Because of their different magnitudes and units, the features, $\left[D_{\parallel}(\omega),D_{\perp}(\omega),\Theta,\Phi,R_1,R_2\right]$, were normalized according to their respective maximal values, detailed in 2.5. Further, the angles $[\Theta,\Phi]$ were wrapped to $[\pi,2\pi]$, respectively, to take the periodicity and inversion symmetry of the orientation space into account.

2.8 | Statistical analysis

Voxelwise RMSE ($RMSE_v$) from the isotropic and anisotropic ROIs within the phantom were grouped according to denoising strategy and compared using one-way ANOVA. In a similar manner, voxelwise EMD from the five subjects were first joined together, grouped according to denoising strategy, and compared using one-way ANOVA. In both phantom and in vivo cases, a multiple comparison test using the Bonferroni correction was performed to determine the effect the different denoising strategies have on the MD-MRI estimates.

3 | RESULTS

3.1 | Diffusion phantom

We first assessed various denoising approaches based on the RMSE of the MD-MRI model fit, considering both isotropic and anisotropic ROIs within the phantom. It is important to note that RMSE serves as a measure of the model's fidelity in capturing the measurements, although it may not independently validate the model. However, when a straightforward physical ground truth is available that is expected to be well-described by the MD-MRI model, as in the case of the phantom, RMSE serves as a robust indicator of the SNR. Figure 3a shows the RMSE of each measurement averaged over all

voxels within each ROI, for each denoising strategy. Especially notable in the isotropic ROI, some volumes have higher fit errors than others, which may indicate more severe image artifacts. However, the $RMSE_m$ remains below 1% of the S_0 signal intensity for all except two volumes in the isotropic ROI, and below 3% in the anisotropic ROI.

Voxelwise RMSE distributions for each ROI and denoising strategy are presented in Figure 3b. One-way ANOVA in the isotropic ROI showed that the source of most mean squares variability was between groups ($p < .00001$), with $RMSE_v$ means of 6.75e−3, 5.72e−3, 3.95e−3, and 4.06e−3, for the Reference, combined data without and with denoising, and TE-based denoising, respectively. Pairwise comparisons using a multiple comparison test with the Bonferroni method identified that all the denoising strategies have significantly different $RMSE_v$ means. Similar analysis was done with the anisotropic ROI voxels, with $RMSE_v$ means of 2.98e−2, 2.45e−2, 1.63e−2, and 1.72e−2, for the Reference, combined data without and with denoising, and TE-based denoising, respectively. Here too, most mean

squares variability was due to differences among the group means ($p < .00001$), and Bonferroni-corrected pairwise comparisons showed that all the denoising strategies have significantly different $RMSE_v$ means. These results demonstrate an advantage toward combining the sparse MD-MRI dataset first, and then applying MPPCA denoising on all the volumes at once.

Next, we illustrate the stability of our efficient MD-MRI acquisition protocol using a well-defined anisotropic phantom. Figure 4a shows the way in which sub-voxel microstructural information is obtained by partitioning the 2D $D_{iso} - D_\Delta^2$ plane into two regions
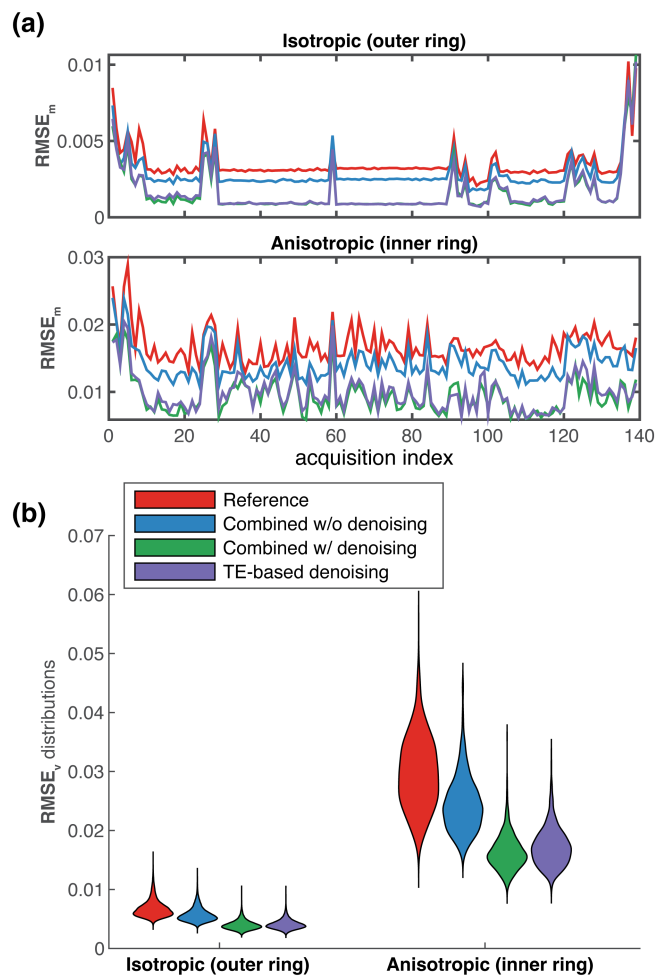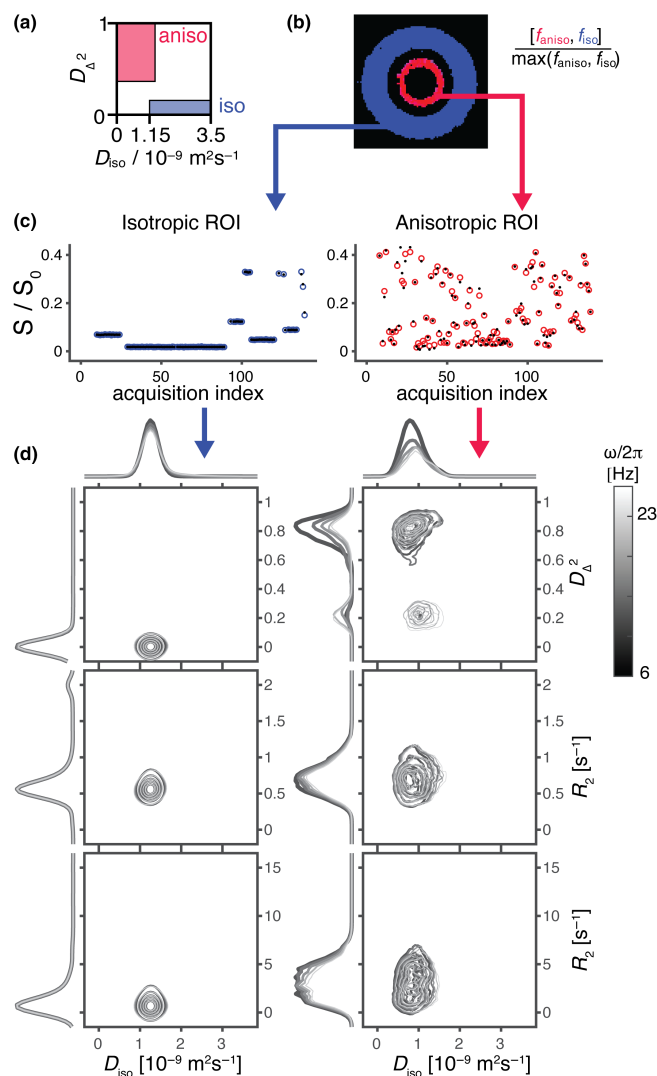

FIGURE 3 Effect of denoising strategy on the model fit root mean square error (RMSE). (a) Normalized RMSE for each measurement (image volume) averaged over the isotropic (top) and anisotropic (bottom) regions of interest (ROIs), color coded according to denoising strategies. (b) Distribution of normalized RMSE over voxels within each ROI, color coded according to denoising strategies.

FIGURE 4 Representative phantom voxels from the isotropic (blue) and anisotropic (red) regions of interest (ROIs). (a) Bin segmentation between the two components representing partial integration regions in the 2D $D_{iso} - D_\Delta^2$ plane. (b) The resulting isotropic and anisotropic signal fraction maps, color-coded (blue = isotropic, red = anisotropic). (c) Single-voxel attenuation profiles (colored circles) and their fits (black dots). (d) $\mathbf{D}(\omega) - R_1 - R_2$ distributions for each voxel projected onto the 2D $D_{iso} - D_\Delta^2$, $D_{iso} - R_1$, and $D_{iso} - R_2$ planes for five frequencies in the range of $\omega/2\pi = 6.6 - 21$ Hz as indicated with the linear gray scale of the contour lines.

(or bins), based on isotropic diffusion length scale and diffusion anisotropy. In the case of the phantom, in which only two well-defined diffusion populations exist, applying the partial integration in Figure 4a in each voxel results in signal fraction map (f_{aniso}, f_{iso}) coded into red and blue colors, respectively, and shown in Figure 4b. Single-voxel attenuation profiles (colored circles) and their fits (black dots) from both ROIs are shown in Figure 4c.

The per-voxel $\mathbf{D}(\omega) - R_1 - R_2$ distributions from both the isotropic and anisotropic ROIs are visualized in Figure 4d as projections onto the 2D $D_{iso} - D_\Delta^2$, $D_{iso} - R_1$, and $D_{iso} - R_2$ planes for frequencies $\omega/2\pi$ between 6.6 and 21 Hz (represented by the grayscale intensity of the contour plots). The microstructural differences between the ROIs are most visible in the $D_{iso} - D_\Delta^2$ projection from a representative single voxel, in which water within the isotropic ROI appears to experience completely isotropic diffusion (D_Δ^2 close to 0), and D_{iso} of about 1.25 μm²/ms, without any notable diffusion frequency dependency. Mostly single peaks in the $D_{iso} - R_1$ and $D_{iso} - R_2$ planes point to low relaxation rates, as expected from aqueous PVP solution (Pierpaoli et al., 2009). The $D_{iso} - D_\Delta^2$ projection from a single voxel within the anisotropic diffusion ROI shows pronounced diffusion frequency/time dependence behavior. A single water population with low D_{iso} of about 0.78 μm²/ms and high D_Δ^2 of about 0.82 is observed at low frequency. A microenvironment with the same D_{iso} but with lower apparent anisotropy (D_Δ^2 of about 0.20) is observed as the frequency increases. Although D_Δ^2 values of about 0.2 have been previously observed in the brain, corresponding to a nearly symmetric "butterfly" spread of components centered about the $D_\Delta = 0$ line (de Almeida Martins et al., 2020; Yon et al., 2020), this inversion-related artifact is not present in our data, as can be seen by the strictly positive D_Δ in Figure S1. Instead, the low anisotropy peak provides direct evidence of the coupling of diffusion length and time scales. This diffusion time/frequency dependency behavior in diffusion phantoms is expected when the asymptotic diffusion time is not reached, and the characteristic length scale, 7.6 μm in our case, cannot be fully sampled. While at 6.6 Hz the diffusion length scale of about 11 μm should fully sample the microstructure, at 21 Hz and a diffusion length scale of about 6 μm, a proportion of the diffusing water is not fully restricted by the boundaries.

Figure 5 displays a compilation of parametric maps representing global and bin-specific statistical characteristics derived from the voxelwise $\mathbf{D}(\omega) - R_1 - R_2$ distributions, preprocessed using all volumes combined for the denoising step. The axial slice of the phantom features two concentric rings: the inner ring, composed of 15 μm diameter fibers in an aqueous solution, exhibits highly anisotropic microstructure, whereas the outer ring contains aqueous PVP solution, known for its isotropic properties.

In Figure 5a, the maps illustrate per-voxel statistics, including means $E[x]$, variances $V[x]$, and covariances $C[x,y]$ for D_{iso}, D_Δ^2, R_1, and R_2, assessed at $\omega/2\pi = 6.6$ Hz. The means $E[D_{iso}]$, $E[R_1]$, and $E[R_2]$ correspond to conventional mean diffusivity (Basser et al., 1994), quantitative R_1, and R_2 (Weiskopf et al., 2021), respectively. The $E\left[D_\Delta^2\right]$ map is akin to metrics used to quantify microscopic diffusion anisotropy (Lasič et al., 2014; Lawrenz et al., 2010; Shemesh et al., 2015).

Averaged across the ROIs, the $E[D_{iso}]$ values were 0.96 ± 0.07 μm²/ms and 1.29 ± 0.01 μm²/ms, for the anisotropic and isotropic ROIs, respectively, in agreement with previous measurements (Laun, Schad, et al., 2009). As expected, the microstructural difference between the ROIs is demonstrated from the averaged anisotropic and isotropic $E\left[D_\Delta^2\right]$ values of 0.63 ± 0.05 and 0.004 ± 0.002, respectively. The increased intravoxel variances in the anisotropic ROI compared with the isotropic region suggest potential heterogeneity and imperfect fiber packing.

Examining the relaxation properties of the phantom, we measured faster transverse relaxation rates in the anisotropic ROI ($E[R_2] = 4.76 \pm 0.77$ and 1.15 ± 0.14 s⁻¹, for the anisotropic and isotropic ROIs, respectively). This observation aligns with expectations of increased relaxation in the presence of polymer fibers due to surface relaxation effects (Laun, Huff, & Stieltjes, 2009). In addition, we observed comparable longitudinal relaxation rates of $E[R_1] = 0.76 \pm 0.05$ and 0.74 ± 0.06 s⁻¹ in the anisotropic and isotropic ROIs, respectively.

The frequency-dependence results, presented in Figure 5b, show the rate of change with frequency within the investigated range of 6.6–21 Hz for the per-voxel means, variances, and covariance of D_{iso} and D_Δ^2. In the $\Delta_{\omega/2\pi} E[D_{iso}]$ map, positive values indicate diffusion time dependency behavior suggestive of restriction (Aggarwal et al., 2012). Conversely, decreased anisotropy with higher frequency results in negative values in the $\Delta_{\omega/2\pi} E\left[D_\Delta^2\right]$ map. In both cases, the phantom regions demonstrated the expected results: positive and negative values of $\Delta_{\omega/2\pi} E[D_{iso}]$ and $\Delta_{\omega/2\pi} E\left[D_\Delta^2\right]$ in the anisotropic ROI, respectively, and negligible frequency dependency in the isotropic ROI.

We can extract subvoxel information from the $D_{iso} - D_\Delta^2$ plane bins depicted in Figure 4a. These bin-resolved maps, displayed in Figure 5c, illustrate the means of the tensorial, relaxation, and frequency properties. Each map employs two orthogonal scales: the brightness intensity reflects the relative signal fraction, while the color scale represents the specific property value. In addition to these metrics, we computed the voxelwise principal orientation of the tensors and visualized it as directionally-encoded color (DEC) maps for each bin, utilizing the tensor orientation data (i.e., $[\Theta, \Phi]$). The DEC map pattern in Figure 5c aligns with findings from previous studies (Laun, Huff, & Stieltjes, 2009; Laun, Schad, et al., 2009).

3.2 | In vivo MD-MRI

We first assessed the impact of different denoising strategies on the MD-MRI pipeline and estimates. Voxelwise agreement between the first and second scan sessions was quantified using the EMD, as detailed in Section 2.7. We calculated EMD histograms for the entire brain averaged across the five subjects for each denoising method, as depicted in Figure 6a. A closer examination of the histogram highlights that denoising the combined MD-MRI data yields the lowest overall EMD values across the entire brain for the five subjects.

Voxelwise EMD distributions for each denoising strategy are presented in Figure 6b. One-way ANOVA showed that the source of
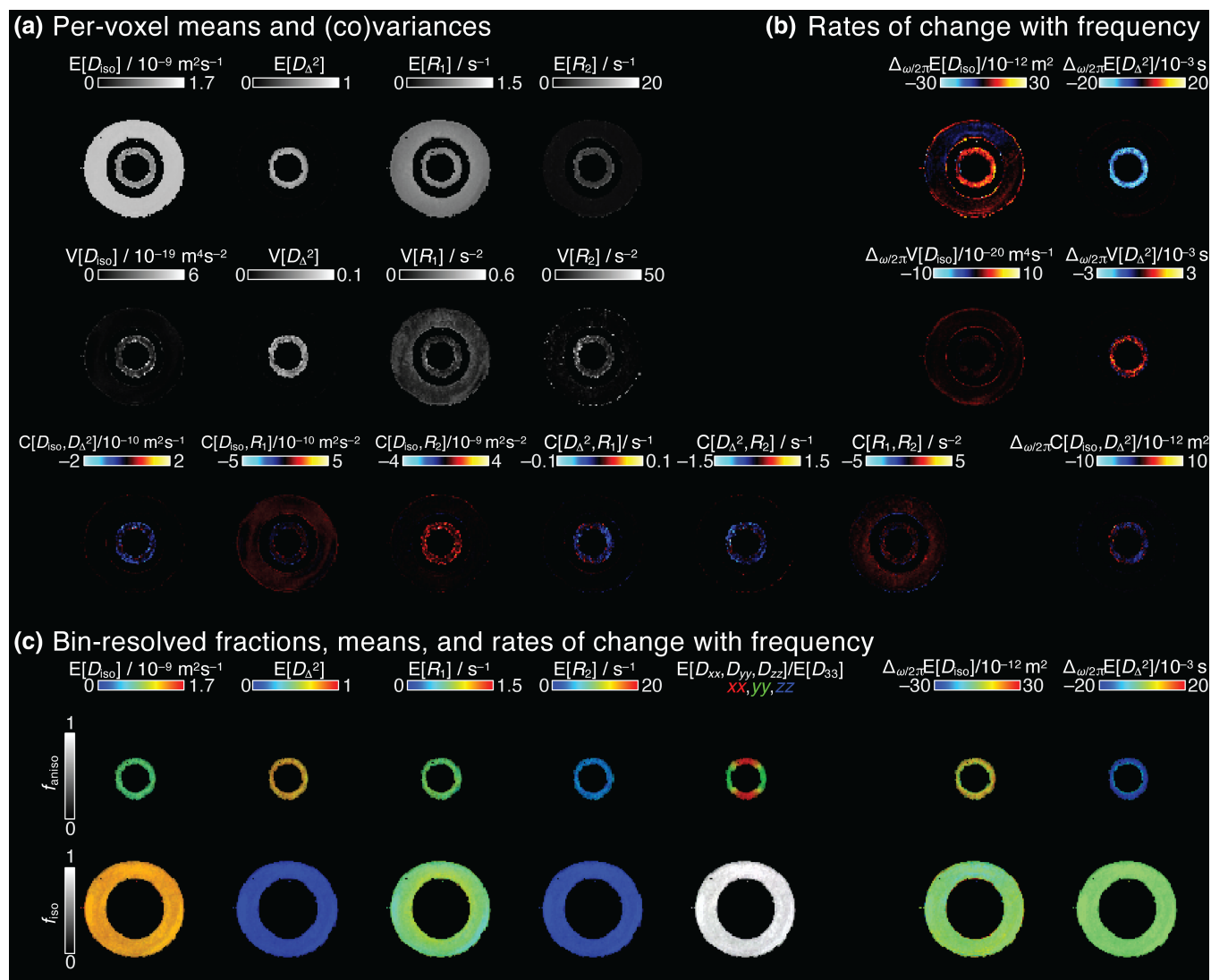
FIGURE 5 Parameter maps of the diffusion phantom derived from voxelwise $\mathbf{D}(\omega) - R_1 - R_2$ distributions. (a) Voxelwise means $E[x]$, variances $V[x]$, and covariances $C[x,y]$ at a selected encoding frequency $\omega/2\pi = 6.6$ Hz. (b) Parameter maps of the rate of change with frequency, $\Delta_{\omega/2\pi}E[x]$. (c) Bin-resolved maps of $E[x]$ and $\Delta_{\omega/2\pi}E[x]$ according to Figure 4a. The brightness and color scales represent, respectively, the signal fractions and the values of each parameter.

most mean squares variability was between groups ($p < .00001$), with EMD means of 3.89e−1, 3.14e−1, 3.10e−1, 3.15e−1 for the Reference, combined data without and with denoising, and TE-based denoising, respectively. Pairwise comparisons using a multiple comparison test with the Bonferroni method revealed that while the EMD obtained from denoising the combined MD-MRI data was significantly lower than the other three strategies, combining the data without denoising and performing TE-based denoising did not significantly alter the EMD.

Figure 6c displays maps of the voxelwise EMD between $\mathbf{D}(\omega) - R_1 - R_2$ distributions at $\omega/2\pi = 6.6$ Hz over two scans from a representative subject using each denoising strategy. High intensities correspond to low $\mathbf{D}(\omega) - R_1 - R_2$ distributions reproducibility. The Reference strategy, that is, no preprocessing at all, produced a large and heterogeneous variability as expected. Although less apparent to

the naked eye, when compared with denoising the combined data strategy, skipping or performing TE-based denoising yielded elevated EMD levels (indicated by white arrows). Raw data images with representative combinations of TE, TR, b-value, and b-tensor rank under the different denoising strategies are shown in Supplementary Figure 2. These analyses support the phantom findings, confirming that the preferred denoising strategy here is to first combine the sparse MD-MRI dataset and then apply MPPCA denoising to all the volumes simultaneously; this approach was adopted for the remainder of this study.

Figure 7 illustrates axial parameter maps derived from voxelwise and bin-resolved statistical descriptors of $\mathbf{D}(\omega) - R_1 - R_2$ distributions assessed at $\omega/2\pi = 6.6$ Hz in a healthy brain. Despite the relatively small number of MD-MRI encoding volumes and higher resolution, the resulting maps exhibit minimal artifacts and align with findings
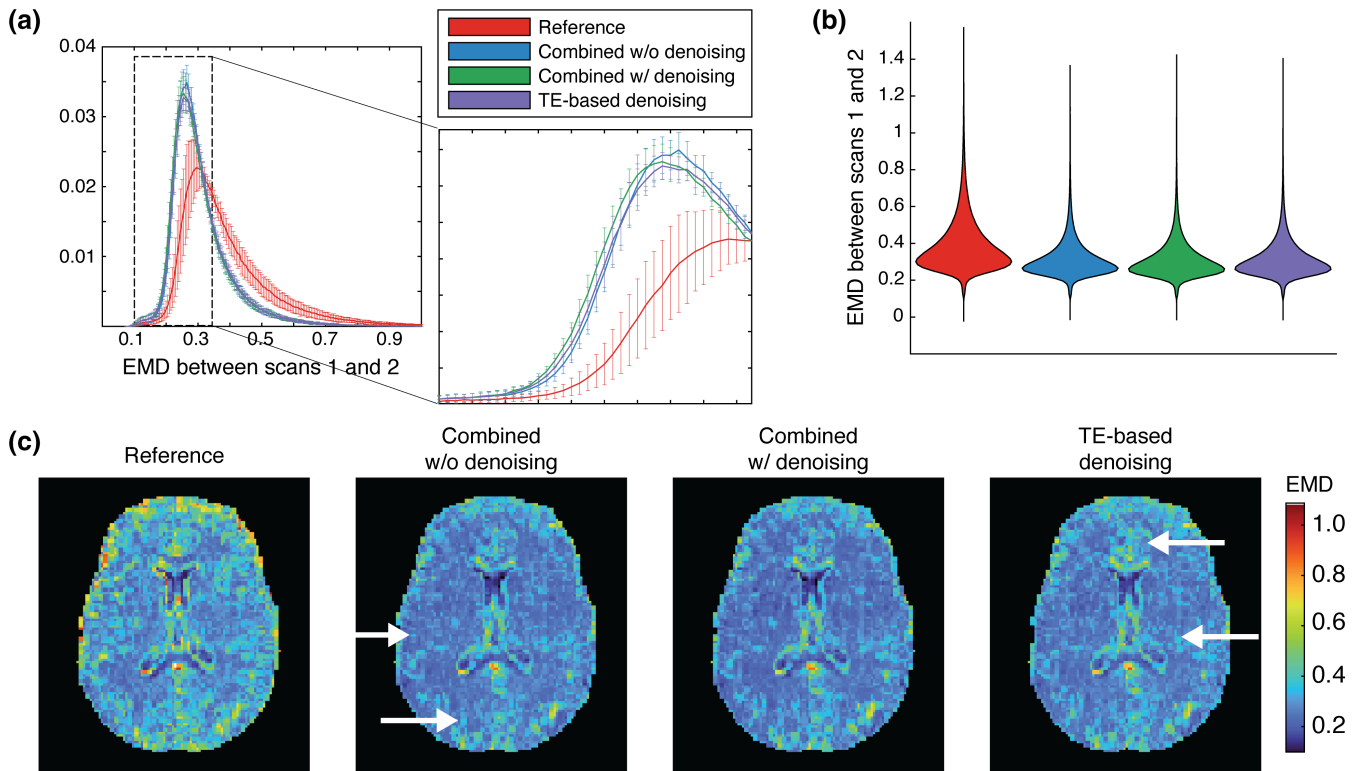
FIGURE 6 Assessing the impact different denoising strategies had on the MD-MRI pipeline and estimates. (a) Whole brain Earth mover's distance (EMD) histograms averaged across the five subjects for each denoising method. Error bars represent standard deviations. (b) Voxelwise EMD distributions across the study population for each denoising strategy. (c) Maps of the voxelwise EMD between $\mathbf{D}(\omega) - R_1 - R_2$ distributions at $\omega = 6.6$ Hz over two scans from a representative subject for each denoising strategy. High intensities correspond to low $\mathbf{D}(\omega) - R_1 - R_2$ distributions reproducibility. White arrows point to the areas with elevated variability.

from prior studies that employed lower-dimensional methods using denser acquisition strategies (de Almeida Martins et al., 2020; Martin et al., 2021; Reymbaut et al., 2021).

Intravoxel information in the human brain can be obtained and mapped by partially integrating regions of the voxelwise $\mathbf{D}(\omega) - R_1 - R_2$ distributions. We chose here to be consistent with previous works and use three regions in the 2D $D_\Delta^2 - D_{iso}$ distribution space that roughly correspond to WM, GM, and CSF, referred to as bin 1, bin 2, and bin 3, respectively, and which are visualized in Figure 7a. When applied voxelwise, partial integration according to these bins results in their respective signal fraction maps, which are visualized as an RGB image, in which red, green, and blue correspond to bins 1, 2, and 3, respectively. The RGB signal fractions map provides intravoxel information, and highlights WM, GM, and CSF contributions, as well as their superpositions.

Similar to previous studies (Martin et al., 2021; Reymbaut et al., 2021), we observed that in voxels containing multiple water populations with distinct diffusion and relaxation properties, intravoxel heterogeneity metrics $V[x]$ and $C[x,y]$ exhibit non-zero values. Consequently, elevated values predominantly appear at tissue interfaces, for example, WM and CSF, with significant parameter variations that can be seen in Figure 7b. In addition to the dominating partial volume effects, the increased $V[x]$ can be caused by contributions from non-Gaussian diffusion effects that violate the GPD assumption

(Jespersen et al., 2019), and induce microscopic kurtosis (Novello et al., 2022). In this case, the microscopic kurtosis is not accounted for in our model, and would appear to split between variances of D_{iso} and D_Δ^2.

The frequency-dependent findings, presented in Figure 7c, illustrate the rate of change with frequency within the examined range of 6.6–21 Hz for voxelwise means, variances, and covariance of D_{iso} and D_Δ^2. As mentioned above, positive $\Delta_{\omega/2\pi}e[D_{iso}]$ values indicate diffusion time dependency behavior suggestive of restriction (Aggarwal et al., 2012), while negative $\Delta_{\omega/2\pi}E\left[D_\Delta^2\right]$ values indicate decreased anisotropy with higher frequency. We observed the highest positive values of $\Delta_{\omega/2\pi}E[D_{iso}]$ in GM, predominantly in the occipital cortex. Negative $\Delta_{\omega/2\pi}E[D_{iso}]$ values, indicative of incoherent CSF flow (Baron & Beaulieu, 2014; Does et al., 2003), were observed in the ventricles. The $\Delta_{\omega/2\pi}E\left[D_\Delta^2\right]$ map exhibited strictly negative values, with the strongest frequency dependency in cerebral WM.

Intravoxel information can be directly imaged by resolving the diffusion and relaxation properties in Figure 7b,c according to the predefined bins. These bin-resolved means of the tensorial, relaxation, and frequency maps are presented in Figure 7d. This analysis parses out the characteristics of predominantly WM, GM, and CSF voxels, for example, relaxation rates and D_Δ^2 anisotropy are markedly higher in WM, compared with GM and CSF. Bin-resolved $\Delta_{\omega/2\pi}E\left[D_\Delta^2\right]$ maps
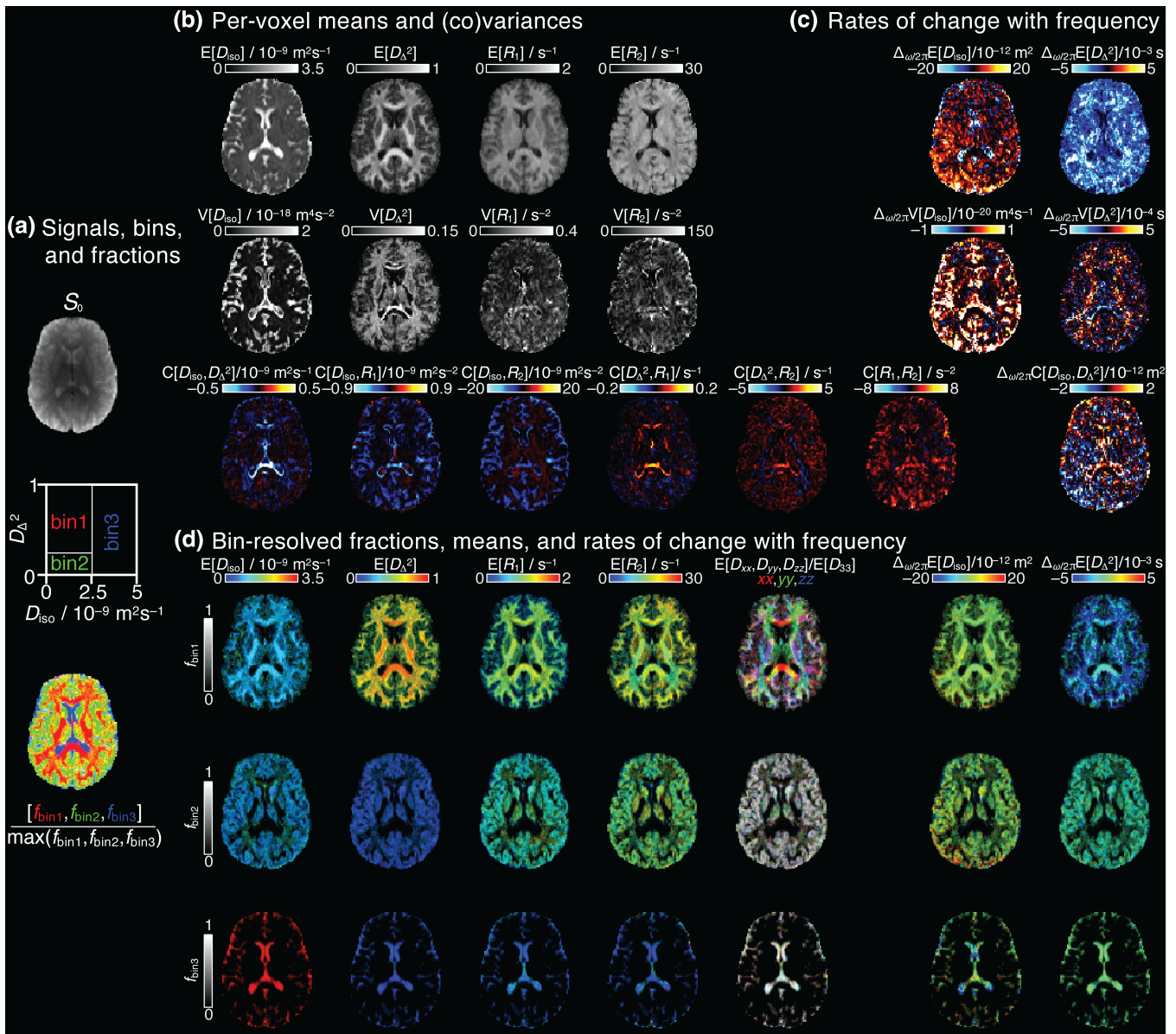
FIGURE 7 Parameter maps of a representative subject derived from voxelwise $\mathbf{D}(\omega) - R_1 - R_2$ distributions. (a) S_0 map displayed in gray scale, diagram with the division of the 2D $D_{iso} - D_{\Delta}^2$ projection into three bins (bin1, bin2, bin3), and the resulting signal fractions ($f_{bin1}, f_{bin2}, f_{bin3}$) coded into RGB color. (b) Per-voxel means $E[x]$, variances $V[x]$, and covariances $C[x, y]$ at a selected encoding frequency $\omega/2\pi = 6.6$ Hz. (c) Parameter maps of the rate of change with frequency, $\Delta_{\omega/2\pi}E[x]$. (d) Bin-resolved maps of $E[x]$ and $\Delta_{\omega/2\pi}E[x]$. The brightness and color scales represent, respectively, the signal fractions and the values of each parameter. EMD, Earth mover's distance.

confirms that indeed cerebral WM regions demonstrate the strongest frequency-dependence of anisotropy.

Whole-brain histograms of bin-resolved means $E[x]$ for each subject and scan are shown in Figure 8. Overall, the data is consistent across all subjects, and especially within repeated measurements. The histogram peaks in Figure 8 align with the visually prominent colors in each bin of Figure 7d. Consistent with previous observations (de Almeida Martins et al., 2020; Martin et al., 2021; Reymbaut et al., 2021), bin 1 consistently exhibits the highest values for $E[R_1]$ and $E[R_2]$, followed closely by bin 2, while big 3 consistently shows substantially lower values.

4 | DISCUSSION

The wealth of information encapsulated within the nonparametric $\mathbf{D}(\omega) - R_1 - R_2$ distributions was demonstrated here using a diffusion phantom and healthy human subjects. Our work was focused on designing and testing a sparse and efficient MD-MRI dataset comprising 139 images, which provides full brain coverage at 2 mm isotropic voxel size, in just 40 min. This work presents a framework that encompasses lower-dimensional methods, that is, 6D $\mathbf{D} - R_1 - R_2$ (Martin et al., 2021), 5D $\mathbf{D} - R_1$ (Reymbaut et al., 2021) and $\mathbf{D} - R_2$ (de Almeida Martins et al., 2020), 4D $\mathbf{D}$ (Topgaard, 2019), and 2D
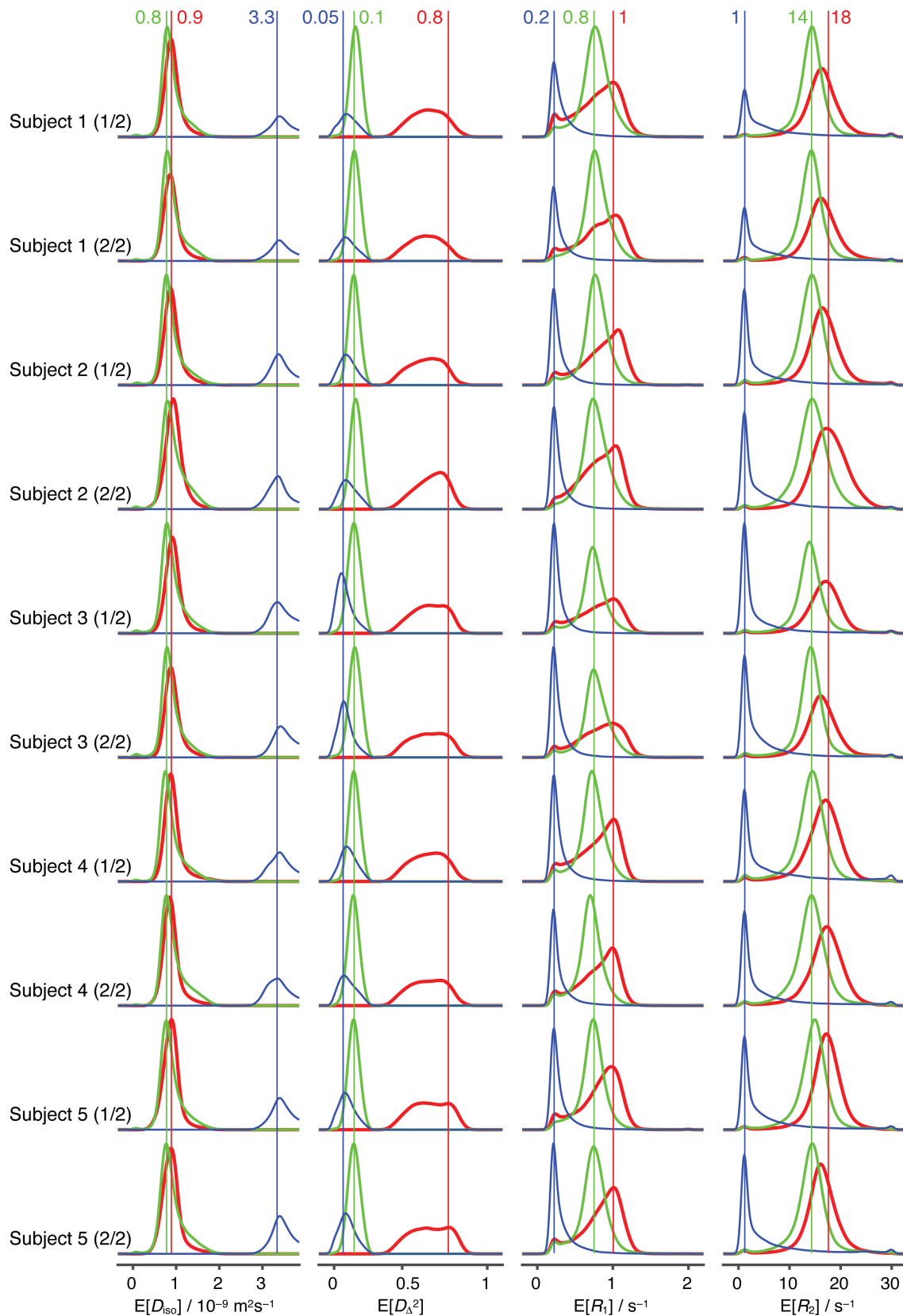
FIGURE 8 Histograms of bin-resolved means $E[x]$ for each measurement. The histograms were obtained from maps like the ones in Figure 7 by evaluating the whole brain and weighting each bin-resolved value of $E[x]$ with its respective signal fraction (f_{bin1}, f_{bin2}, f_{bin3}), using a narrow Gaussian kernel. The red, green, and blue traces report data for the bins one to three, loosely corresponding to white matter, gray matter, and CSF, and the similarly colored vertical lines and numbers indicate visually estimated representative parameter values across all subjects and repetitions. All subjects were scanned twice.

distributions (English et al., 1991; Kim et al., 2017; Pas et al., 2020), while including a diffusion time/frequency dependency that unlocks unique information. The efficient acquisition design prompted an inquiry into the denoising of sparse MD data, a question we have methodically explored.

Utilizing the inherent spectral content of the diffusion gradient waveforms to explore the frequency dependence of the diffusion tensor distribution and their correlations with R_1 and R_2, may provide crucial missing information regarding the diffusion time-dependency in biological tissue (Burcaw et al., 2015; Fieremans et al., 2016), via a unified, (biophysical) model-free framework. While conventional oscillating gradient spin echo (OGSE) protocols (Stepišnik, 1981, 1985) can reach a maximum frequency of 60 Hz using clinical scanners (Arbabi et al., 2020), the numerically optimized linear, planar, and spherical b-tensors utilized in our study, while limited to a diffusion frequency range of 6.6–21 Hz with current standard hardware, offer distinct advantages. These rank 2 and 3 b-tensors are able to encode diffusion correlations (Mitra, 1995), and thus to generate the full-rank diffusion covariance tensor (Benjamini et al., 2012; Ning et al., 2021; Westin et al., 2014), setting them apart from OGSE-based techniques (Baron & Beaulieu, 2014; Xu et al., 2016). Consequently, we have demonstrated how this frequency dependency can be dissected into intravoxel components based on their $\mathbf{D}(\omega) - R_1 - R_2$ distribution, enabling the creation of microstructure-specific maps.

Although high-dimensional data is expected to contain redundancies that could be leveraged in MPPCA denoising (Olesen et al., 2023), the validity of this assertion toward the sparse MD-MRI protocol we present here had to be examined. We used the RMSE of the MD-MRI model fit from the isotropic and anisotropic ROIs within the phantom to assess the performance of several denoising strategies: denoising the diffusion data for each TE separately (Veraart et al., 2018), denoising the full MD data, and skipping the denoising step altogether. The results showed, as expected and previously demonstrated (Does et al., 2019; Schilling et al., 2023), that MPPCA denoising improves the overall performance, while indicating an advantage toward denoising the full MD data over the other strategies (Figure 3). We used a conservative choice of the denoising window based on the original recommendation (Veraart, Novikov, et al., 2016). Such a choice, which translates to relatively small window sizes in the case of our sparse data acquisition, also avoids unwanted bias and reduced sensitivity in the output, as was recently shown (Fernandes et al., 2023).

A diffusion phantom was then used to demonstrate the robustness of the sparse imaging protocol and processing pipeline, and to illustrate how the high dimensional diffusion-relaxation information can be linked to a priori known and well-characterized microstructure. Full distributions from single voxels in the two distinct phantom ROIs were projected onto 2D $D_{iso} - D_\Delta^2$, $D_{iso} - R_1$, and $D_{iso} - R_2$ planes (Figure 4). These lower-dimensional distributions showed how the microstructural information is robustly captured via distinct spectral signatures for the isotropic and anisotropic regions of the phantom. Further, the frequency dependence of D_{iso} and D_Δ^2 was clearly exhibited: water restricted between the fibers experience reduced interactions with barriers in the short diffusion time regime (high ω), resulting in increased apparent D_{iso} and in the rise of a water population with

decreased anisotropy D_Δ^2. The appearance of a low diffusion anisotropy peak at high frequency provides direct evidence of the coupling of diffusion length and time scales. With assumed hexagonal close packing of the phantom's fibers (Laun, Huff, & Stieltjes, 2009), the physical characteristic length scale is about 7.6 μm, while the diffusion length scales in the phantom are about 6 and 11 μm for 21 and 6.6 Hz, respectively. And indeed, these numbers are supported by the relatively unrestricted water population seen at the high end of the frequency range, which vanishes as the diffusion length scale becomes greater than the physical characteristic length scale.

First and second-order statistical descriptors of D_{iso}, D_Δ^2, R_1, and R_2 were used to summarize and visualize aspects of the phantom voxelwise 6D distributions in a straightforward manner (Figure 5). These maps were all in accordance with the expected diffusion and relaxation values (Laun, Huff, & Stieltjes, 2009). The frequency-dependence map of $\Delta_{\omega/2\pi}E[D_{iso}]$ is equivalent to Δ_f ADC measured with OGSE (Aggarwal et al., 2012; Kershaw et al., 2013), and showed no frequency-dependence in the isotropic ROI but did show positive values in the anisotropic ROIs, as expected due to restriction. Similarly, the $\Delta_{\omega/2\pi}E\left[D_\Delta^2\right]$ map showed no frequency-dependence in the isotropic ROI but showed negative values in the anisotropic ROIs, which is expected because the diffusion length scale at $\omega/2\pi = 21$ Hz is smaller than the nominal characteristic length scale of the phantom, described above.

We further assessed the performance of the investigated denoising strategies using in vivo human data to complement the results obtained from the phantom study. We conducted scans on five control subjects, which is close to the median sample size of six reported for technical MRI studies (Hanspach et al., 2021), each scanned twice with a few weeks in between, and quantified the variability of voxelwise $\mathbf{D}(\omega) - R_1 - R_2$ distributions between scans under different denoising strategies. The results, depicted in Figure 6, reaffirm the conclusions drawn from the phantom-based experiments. Specifically, they highlight the preference for denoising the complete MD dataset when dealing with sparsely encoded data. While taking advantage of the inherent redundancy in each dimension of multidimensional data can enhance noise removal (Olesen et al., 2023), it necessitates sampling across diffusion and relaxation dimensions in a grid-like pattern. Our efficient MD-MRI acquisition protocol does not meet these conditions, as explained in the Introduction.

Parameter maps, presented in Figure 7, such as $E[D_{iso}]$ and $E\left[D_\Delta^2\right]$ show similar trends as in previous in vivo human brain studies (de Almeida Martins et al., 2020; Martin et al., 2021; Reymbaut et al., 2021). As expected, bin-resolved $E[D_{iso}]$, $E\left[D_\Delta^2\right]$, $E[R_1]$, and $E[R_2]$ all show larger values in WM (bin 1) compared with GM (bin 2). It is crucial to consider the time and length scales defined by the diffusion-encoding gradients for interpretation of the frequency dependence maps. In this work, our sampling scheme included centroid frequencies varying from 6.6 to 21 Hz (see Figure 1), which can be used to explore restricted diffusion. The current frequency content range is expected to be particularly sensitive to length scale of ~13 μm (if spherical geometry is assumed; Stepišnik, 1993; Woessner, 1963). Therefore, the observed elevated values of $\Delta_{\omega/2\pi}E[D_{iso}]$ in deep WM and cortical brain regions should be considered with respect to the

probed length scale of 13 μm, which would be in line with neuronal soma dimensions in the human cortex (Rajkowska et al., 1998). Elevated $\Delta_{\omega/2\pi} E[D_{iso}]$ values were also hypothesized to indicate increased local tissue disorder (Arbabi et al., 2020), which supports our findings of lower frequency dependence in WM tracts compared with subcortical WM and cortical GM. Negative $\Delta_{\omega/2\pi} E[D_{iso}]$ values were observed in the ventricles, indicative of incoherent CSF flow (Baron & Beaulieu, 2014; Does et al., 2003).

Basic considerations in the pulse sequence and acquisition design prevent quantitative R_1 and R_2 comparisons with different studies. When considering the current relaxation encoding, the measured signal arises from a complex interplay involving partial excitation by radiofrequency pulses, relaxation processes, and exchange phenomena among multiple proton pools, each possessing unique MR properties related to R_1, R_2, and linewidth (Manning et al., 2021). These complex relationships make the measured R_1 and to a lesser extent, the R_2, dependent upon the particular choice of pulse sequence, slice thickness, and radiofrequency pulses bandwidth. Specifically, we see this effect in Figure 8, in which R_1 values are higher than previously presented using a different imaging protocol. In addition, diffusion gradient hardware limitations constrained the minimal TE in this study to 40 ms, in which myelin water (with R_2 of $\sim100\,s^{-1}$) is expected to be fully attenuated (Manning et al., 2021). Reducing the minimal echo time can be achieved by, for example, implementing spiral sampling of k-space (Lee, Wilm, et al., 2021) or using next-generation diffusion gradients (Huang et al., 2021).

The framework we present here is best suited when biophysical model-based approaches may not be applicable (Novikov et al., 2018), in which the information on the underlying tissue composition is not available beforehand. The most likely scenarios would involve pathological tissue resulting from a wide range of neurological conditions such as neurodegeneration, neuroinflammation, cancer, or even in normal aging. And indeed, diffusion-relaxation MD-MRI has been recently gaining momentum, showing that it is uniquely positioned to address a range of challenging biological questions such as prostate cancer (Wei et al., 2022; Zhang et al., 2020), breast cancer (Naranjo et al., 2021), placenta characterization (Slator et al., 2019), spinal cord injury (Benjamini et al., 2020; Kim et al., 2017), axonal injury (Benjamini et al., 2021), and astrogliosis (Benjamini et al., 2022).

5 | CONCLUSION

This study establishes the feasibility of $\mathbf{D}(\omega) - R_1 - R_2$ correlation, combining diffusion-relaxation weighting, time/frequency dependence, and tensor-valued encoding, using an efficient 40-min protocol with full brain coverage at 2 mm³ voxel size. The MD-MRI framework provides rich intravoxel information, without presuming tissue composition, of high-dimensional correlations of relaxation and diffusion properties, offering insights into cell types, chemical composition, axonal density, restriction, and orientations within a voxel. We demonstrated that this experimental design and acquisition protocol, in conjunction with the

MD-MRI processing pipeline, produce robust estimates, encouraging the broader adoption and use of this new imaging approach in characterizing both healthy and pathological tissues.

CONFLICT OF INTEREST STATEMENT

The authors declare no conflict of interest.

DATA AVAILABILITY STATEMENT

The data that support the findings of this study are available on request from the corresponding author. The data are not publicly available due to privacy or ethical restrictions.

ORCID

Dan Benjamini 🅳 https://orcid.org/0000-0002-9558-7056

REFERENCES

Aggarwal, M., Jones, M. V., Calabresi, P. A., Mori, S., & Zhang, J. (2012). Probing mouse brain microstructure using oscillating gradient diffusion MRI. *Magnetic Resonance in Medicine*, *67*, 98–109. https://doi.org/10.1002/mrm.22981

Arbabi, A., Kai, J., Khan, A. R., & Baron, C. A. (2020). Diffusion dispersion imaging: Mapping oscillating gradient spin-echo frequency dependence in the human brain. *Magnetic Resonance in Medicine*, *83*, 2197–2208. https://doi.org/10.1002/mrm.28083

Baron, C. A., & Beaulieu, C. (2014). Oscillating gradient spin-echo (OGSE) diffusion tensor imaging of the human brain. *Magnetic Resonance in Medicine*, *72*, 726–736. https://doi.org/10.1002/mrm.24987

Basser, P. J., Mattiello, J., & LeBihan, D. (1994). MR diffusion tensor spectroscopy and imaging. *Biophysical Journal*, *66*, 259–267. https://doi.org/10.1016/S0006-3495(94)80775-1

Beaulieu, C. (2002). The basis of anisotropic water diffusion in the nervous system—A technical review. *NMR in Biomedicine*, *15*, 435–455. https://doi.org/10.1002/nbm.782

Benjamini, D. (2020). *Nonparametric inversion of relaxation and diffusion correlation data*. Royal Society of Chemistry. https://doi.org/10.1039/9781788019910-00278

Benjamini, D., & Basser, P. J. (2017). Magnetic resonance microdynamic imaging reveals distinct tissue microenvironments. *NeuroImage*, *163*, 183–196. https://doi.org/10.1016/j.neuroimage.2017.09.033

Benjamini, D., & Basser, P. J. (2020). Multidimensional correlation MRI. *NMR in Biomedicine*, *33*, e4226. https://doi.org/10.1002/nbm.4226

Benjamini, D., Hutchinson, E. B., Komlosh, M. E., Comrie, C. J., Schwerin, S. C., Zhang, G., Pierpaoli, C., & Basser, P. J. (2020). Direct and specific assessment of axonal injury and spinal cord microenvironments using diffusion correlation imaging. *NeuroImage*, *221*, 117195. https://doi.org/10.1016/j.neuroimage.2020.117195

Benjamini, D., Iacono, D., Komlosh, M. E., Perl, D. P., Brody, D. L., & Basser, P. J. (2021). Diffuse axonal injury has a characteristic multidimensional MRI signature in the human brain. *Brain*, *144*, 800–816. https://doi.org/10.1093/brain/awaa447

Benjamini, D., Katz, Y., & Nevo, U. (2012). A proposed 2D framework for estimation of pore size distribution by double pulsed field gradient NMR. *The Journal of Chemical Physics*, *137*, 224201. https://doi.org/10.1063/1.4769792

Benjamini, D., Priemer, D. S., Perl, D. P., Brody, D. L., & Basser, P. J. (2022). Mapping astrogliosis in the individual human brain using multidimensional MRI. *Brain*, 146, 1212–1226. https://doi.org/10.1093/brain/awac298

Bouhrara, M., Rejimon, A. C., Cortina, L. E., Khattar, N., Bergeron, C. M., Ferrucci, L., Resnick, S. M., & Spencer, R. G. (2020). Adult brain aging investigated using BMC-mcdespot-based myelin water fraction imaging. *Neurobiology of Aging*, 85, 131–139. https://doi.org/10.1016/j.neurobiolaging.2019.10.003

Burcaw, L. M., Fieremans, E., & Novikov, D. S. (2015). Mesoscopic structure of neuronal tracts from timedependent diffusion. *NeuroImage*, 114, 18–37. https://doi.org/10.1016/j.neuroimage.2015.03.061

Conturo, T. E., McKinstry, R. C., Akbudak, E., & Robinson, B. H. (1996). Encoding of anisotropic diffusion with tetrahedral gradients: A general mathematical diffusion formalism and experimental results. *Magnetic Resonance in Medicine*, 35, 399–412. https://doi.org/10.1002/mrm.1910350319

de Almeida Martins, J. P., Tax, C. M. W., Szczepankiewicz, F., Jones, D. K., Westin, C.-F., & Topgaard, D. (2020). Transferring principles of solid-state and laplace NMR to the field of in vivo brain MRI. *Magnetic Resonance*, 1, 27–43. https://doi.org/10.5194/mr-1-27-2020

de Almeida Martins, J. P., & Topgaard, D. (2018). Multidimensional correlation of nuclear relaxation rates and diffusion tensors for model-free investigations of heterogeneous anisotropic porous materials. *Scientific Reports*, 8, 2488. https://doi.org/10.1038/s41598-018-19826-9

DeSantis, S., Barazany, D., Jones, D. K., & Assaf, Y. (2016). Resolving relaxometry and diffusion properties within the same voxel in the presence of crossing fibres by combining inversion recovery and diffusion-weighted acquisitions. *Magnetic Resonance in Medicine*, 75, 372–380. https://doi.org/10.1002/mrm.25644

Does, M. D., & Gore, J. C. (2002). Compartmental study of T1 and T2 in rat brain and trigeminal nerve in vivo. *Magnetic Resonance in Medicine*, 47, 274–283. https://doi.org/10.1002/mrm.10060

Does, M. D., Olesen, J. L., Harkins, K. D., Serradas-Duarte, T., Gochberg, D. F., Jespersen, S. N., & Shemesh, N. (2019). Evaluation of principal component analysis image denoising on multi-exponential MRI relaxometry. *Magnetic Resonance in Medicine*, 81, 3503–3514. https://doi.org/10.1002/mrm.27658

Does, M. D., Parsons, E. C., & Gore, J. C. (2003). Oscillating gradient measurements of water diffusion in normal and globally ischemic rat brain. *Magnetic Resonance in Medicine*, 49, 206–215. https://doi.org/10.1002/mrm.10385

Dvorak, A. V., Swift-LaPointe, T., Vavasour, I. M., Lee, L. E., Abel, S., Russell-Schulz, B., Graf, C., Wurl, A., Liu, H., Laule, C., Li, D. K. B., Traboulsee, A., Tam, R., Boyd, L. A., MacKay, A. L., & Kolind, S. H. (2021). An atlas for human brain myelin content throughout the adult life span. *Scientific Reports*, 11, 269. https://doi.org/10.1038/s41598-020-79540-3

English, A. E., Whittall, K. P., Joy, M. L. G., & Henkelman, R. M. (1991). Quantitative two-dimensional time correlation relaxometry. *Magnetic Resonance in Medicine*, 22, 425–434. https://doi.org/10.1002/mrm.1910220250

Fernandes, F. F., Olesen, J. L., Jespersen, S. N., & Shemesh, N. (2023). MP-PCA denoising of fMRI time-series data can lead to artificial activation "spreading". *NeuroImage*, 273, 120118. https://doi.org/10.1016/j.neuroimage.2023.120118

Fieremans, E., Burcaw, L. M., Lee, H.-H., Lemberskiy, G., Veraart, J., & Novikov, D. S. (2016). In vivo observation and biophysical interpretation of time-dependent diffusion in human white matter. *NeuroImage*, 129, 414–427. https://doi.org/10.1016/j.neuroimage.2016.01.018

Hanspach, J., Nagel, A. M., Hensel, B., Uder, M., Koros, L., & Laun, F. B. (2021). Sample size estimation: Current practice and considerations for original investigations in MRI technical development studies. *Magnetic Resonance in Medicine*, 85, 2109–2116. https://doi.org/10.1002/mrm.28550

Huang, S. Y., Witzel, T., Keil, B., Scholz, A., Davids, M., Dietz, P., Rummert, E., Ramb, R., Kirsch, J. E., Yendiki, A., Fan, Q., Tian, Q., Ramos-Llordén, G., Lee, H. H., Nummenmaa, A., Bilgic, B., Setsompop, K., Wang, F., Avram, A. V., ... Rosen, B. R. (2021). Connectome 2.0: Developing the next-generation ultra-high gradient strength human MRI scanner for bridging studies of the micro-, meso- and macro-connectome. *NeuroImage*, 243, 118530. https://doi.org/10.1016/j.neuroimage.2021.118530

Hurlimann, M. D., Burcaw, L., & Song, Y.-Q. (2006). Quantitative characterization of food products by twodimensional D–and–distribution functions in a static gradient. *Journal of Colloid and Interface Science*, 297, 303–311. https://doi.org/10.1016/j.jcis.2005.10.047

Irfanoglu, M., Nayak, A., Taylor, P., & Pierpaoli, C. (2023). Tortoise v4: Reimagining the nih diffusion MRI processing pipeline.

Irfanoglu, M. O., Modi, P., Nayak, A., Hutchinson, E. B., Sarlls, J., & Pierpaoli, C. (2015). Dr-Buddi (diffeomorphic registration for blip-up blip-down diffusion imaging) method for correcting echo planar imaging distortions. *NeuroImage*, 106, 284–299. https://doi.org/10.1016/j.neuroimage.2014.11.042

Jespersen, S. N., Olesen, J. L., Ianuş, A., & Shemesh, N. (2019). Effects of nongaussian diffusion on "isotropic diffusion" measurements: An ex-vivo microimaging and simulation study. *Journal of Magnetic Resonance*, 300, 84–94. https://doi.org/10.1016/j.jmr.2019.01.007

Kellner, E., Dhital, B., Kiselev, V. G., & Reisert, M. (2016). Gibbs-ringing artifact removal based on local subvoxel-shifts. *Magnetic Resonance in Medicine*, 76, 1574–1581. https://doi.org/10.1002/mrm.26054

Kershaw, J., Leuze, C., Aoki, I., Obata, T., Kanno, I., Ito, H., Yamaguchi, Y., & Handa, H. (2013). Systematic changes to the apparent diffusion tensor of in vivo rat brain measured with an oscillating-gradient spin-echo sequence. *NeuroImage*, 70, 10–20. https://doi.org/10.1016/j.neuroimage.2012.12.036

Kim, D., Doyle, E. K., Wisnowski, J. L., Kim, J. H., & Haldar, J. P. (2017). Diffusion-relaxation correlation spectroscopic imaging: A multidimensional approach for probing microstructure. *Magnetic Resonance in Medicine*, 78, 2236–2249. https://doi.org/10.1002/mrm.26629

Komlosh, M. E., Benjamini, D., Hutchinson, E. B., King, S., Haber, M., Avram, A. V., Holtzclaw, L. A., Desai, A., Pierpaoli, C., & Basser, P. J. (2018). Using double pulsed-field gradient MRI to study tissue microstructure in traumatic brain injury (TBI). *Microporous and Mesoporous Materials*, 269, 156–159. https://doi.org/10.1016/j.micromeso.2017.05.030

Kundu, S., Barsoum, S., Ariza, J., Nolan, A. L., Latimer, C. S., Keene, C. D., Basser, P. J., & Benjamini, D. (2023). Mapping the individual human cortex using multidimensional MRI and unsupervised learning. *Brain Communications*, 5, fcad258. https://doi.org/10.1093/braincomms/fcad258

Labadie, C., Lee, J.-H., Rooney, W. D., Jarchow, S., Aubert-Frecon, M., Springer, C. S., & Moller, H. E. (2014). Myelin water mapping by spatially regularized longitudinal relaxographic imaging at high magnetic fields. *Magnetic Resonance in Medicine*, 71, 375–387. https://doi.org/10.1002/mrm.24670

Lasič, S., Szczepankiewicz, F., Eriksson, S., Nilsson, M., & Topgaard, D. (2014). Microanisotropy imaging: Quantification of microscopic diffusion anisotropy and orientational order parameter by diffusion MRI with magicangle spinning of the q-vector. *Frontiers in Physics*, 2, 11. https://doi.org/10.3389/fphy.2014.00011

Lasič, S., Yuldasheva, N., Szczepankiewicz, F., Nilsson, M., Budde, M., Dall'Armellina, E., Schneider, J. E., Teh, I., & Lundell, H. (2022). Stay on the beat with tensor-valued encoding: Time-dependent diffusion and cell size estimation in ex vivo heart. *Frontiers in Physics*, 10, 812115. https://doi.org/10.3389/fphy.2022.812115

Laun, F. B., Huff, S., & Stieltjes, B. (2009). On the effects of dephasing due to local gradients in diffusion tensor imaging experiments: Relevance for diffusion tensor imaging fiber phantoms. *Magnetic Resonance Imaging*, 27, 541–548. https://doi.org/10.1016/j.mri.2008.08.011

Laun, F. B., Schad, L. R., Klein, J., & Stieltjes, B. (2009). How background noise shifts eigenvectors and increases eigenvalues in DTI. *Magnetic Resonance Materials in Physics, Biology and Medicine*, 22, 151–158. https://doi.org/10.1007/s10334-008-0159-6

Lawrenz, M., Koch, M. A., & Finsterbusch, J. (2010). A tensor model and measures of microscopic anisotropy for double-wave-vector diffusion-weighting experiments with long mixing times. *Journal of Magnetic Resonance*, 202, 43–56. https://doi.org/10.1016/j.jmr.2009.09.015

LeBihan, D. (1990). Diffusion/perfusion MR imaging of the brain: From structure to function. *Radiology*, 177, 328–329. https://doi.org/10.1148/radiology.177.2.2217762

Lee, H., Novikov, D. S., & Fieremans, E. (2021). Removal of partial fourier-induced GIBBS (RPG) ringing artifacts in MRI. *Magnetic Resonance in Medicine*, 86, 2733–2750. https://doi.org/10.1002/mrm.28830

Lee, Y., Wilm, B. J., Brunner, D. O., Gross, S., Schmid, T., Nagy, Z., & Pruessmann, K. P. (2021). On the signal-to-noise ratio benefit of spiral acquisition in diffusion MRI. *Magnetic Resonance in Medicine*, 85, 1924–1937. https://doi.org/10.1002/mrm.28554

Leuze, C., Aswendt, M., Ferenczi, E., Liu, C. W., Hsueh, B., Goubran, M., Tian, Q., Steinberg, G., Zeineh, M. M., Deisseroth, K., & McNab, J. A. (2017). The separate effects of lipids and proteins on brain MRI contrast revealed through tissue clearing. *NeuroImage*, 156, 412–422. https://doi.org/10.1016/j.neuroimage.2017.04.021

Lundell, H., & Lasic, S. (2020). Chapter 2. Diffusion encoding with general gradient waveforms. https://doi.org/10.1039/9781788019910-00012

Lundell, H., & Lasič, S. (2020). Diffusion encoding with general gradient waveforms. In D. Topgaard (Ed.), *Advanced diffusion encoding methods in MRI: New developments in NMR* (pp. 12–67). Royal Society of Chemistry. https://doi.org/10.1039/9781788019910-00012

Mackay, A., Whittall, K., Adler, J., Li, D., Paty, D., & Graeb, D. (1994). In vivo visualization of myelin water in brain by magnetic resonance. *Magnetic Resonance in Medicine*, 31, 673–677. https://doi.org/10.1002/mrm.1910310614

Manning, A. P., MacKay, A. L., & Michal, C. A. (2021). Understanding aqueous and non-aqueous proton T1 relaxation in brain. *Journal of Magnetic Resonance*, 323, 106909. https://doi.org/10.1016/j.jmr.2020.106909

Martin, J., Reymbaut, A., Schmidt, M., Doerfler, A., Uder, M., Laun, F. B., & Topgaard, D. (2021). Nonparametric D-R1-R2 distribution MRI of the living human brain. *NeuroImage*, 245, 118753. https://doi.org/10.1016/j.neuroimage.2021.118753

Mitra, P. (1995). Multiple wave-vector extensions of the nmr pulsed-field-gradient spin-echo diffusion measurement. *Physical Review B*, 51, 15074–15078.

Naranjo, I. D., Reymbaut, A., Brynolfsson, P., Lo Gullo, R., Bryskhe, K., Topgaard, D., Giri, D. D., Reiner, J. S., Thakur, S. B., & Pinker-Domenig, K. (2021). Multidimensional diffusion magnetic resonance imaging for characterization of tissue microstructure in breast cancer patients: A prospective pilot study. *Cancers*, 13(7), 1606.

Narvaez, O., Svenningsson, L., Yon, M., Sierra, A., & Topgaard, D. (2022). Massively multidimensional diffusion-relaxation correlation MRI. *Frontiers in Physics*, 9, 793966. https://doi.org/10.3389/fphy.2021.793966

Narvaez, O., Yon, M., Jiang, H., Bernin, D., Forssell-Aronsson, E., Sierra, A., & Topgaard, D. (2021). Model-free approach to the interpretation of restricted and anisotropic self-diffusion in magnetic resonance of biological tissues. arXiv. https://doi.org/10.48550/arxiv.2111.07827

Neuman, C. H. (1974). Spin echo of spins diffusing in a bounded medium. *The Journal of Chemical Physics*, 60, 4508–4511. https://doi.org/10.1063/1.1680931

Nilsson, M., Szczepankiewicz, F., Lampinen, B., Ahlgren, A., de Almeida Martins, J. P., Lasic, S., Westin, C. F., & Topgaard, D. (2018). An open-source framework for analysis of multidimensional diffusion MRI data implemented in matlab.

Ning, L., Szczepankiewicz, F., Nilsson, M., Rathi, Y., & Westin, C.-F. (2021). Probing tissue microstructure by diffusion skewness tensor imaging. *Scientific Reports*, 11, 135. https://doi.org/10.1038/s41598-020-79748-3

Novello, L., Henriques, R. N., Ianuş, A., Feiweier, T., Shemesh, N., & Jovicich, J. (2022). In vivo correlation tensor MRI reveals microscopic kurtosis in the human brain on a clinical 3T scanner. *NeuroImage*, 254, 119137. https://doi.org/10.1016/j.neuroimage.2022.119137

Novikov, D. S., Fieremans, E., Jespersen, S. N., & Kiselev, V. G. (2019). Quantifying brain microstructure with diffusion MRI: Theory and parameter estimation. *NMR in Biomedicine*, 32, e3998. https://doi.org/10.1002/nbm.3998

Novikov, D. S., Kiselev, V. G., & Jespersen, S. N. (2018). On modeling. *Magnetic Resonance in Medicine*, 79, 3172–3193. https://doi.org/10.1002/mrm.27101

Olesen, J. L., Ianus, A., Ostergaard, L., Shemesh, N., & Jespersen, S. N. (2023). Tensor denoising of multidimensional MRI data. *Magnetic Resonance in Medicine*, 89, 1160–1172. https://doi.org/10.1002/mrm.29478

Osadebey, M., Pedersen, M., Arnold, D., & Wendel-Mitoraj, K. (2019). Local indicators of spatial autocorrelation (LISA): Application to blind noise-based perceptual quality metric index for magnetic resonance images. *Journal of Imaging*, 5, 20. https://doi.org/10.3390/jimaging5010020

Pas, K., Komlosh, M. E., Perl, D. P., Basser, P. J., & Benjamini, D. (2020). Retaining information from multidimensional correlation MRI using a spectral regions of interest generator. *Scientific Reports*, 10, 3246. https://doi.org/10.1038/s41598-020-60092-5

Peled, S., Cory, D. G., Raymond, S. A., Kirschner, D. A., & Jolesz, F. A. (1999). Water diffusion, T(2), and compartmentation in frog sciatic nerve. *Magnetic Resonance in Medicine*, 42, 911–918.

Pierpaoli, C., Barnett, A., Basser, P., Chang, L.-C., Koay, C., Pajevic, S., Rohde, G., Sarlls, J., & Wu, M. (2010). Tortoise: An integrated software package for processing of diffusion MRI data.

Pierpaoli, C., Jezzard, P., Basser, P. J., Barnett, A., & Chiro, G. D. (1996). Diffusion tensor mr imaging of the human brain. *Radiology*, 201, 637–648. https://doi.org/10.1148/radiology.201.3.8939209

Pierpaoli, C., Sarlls, J., Nevo, U., Basser, P. J., & Horkay, F. (2009). Polyvinylpyrrolidone (PVP) water solutions as isotropic phantoms for diffusion MRI studies.

Pizzolato, M., Palombo, M., Bonet-Carne, E., Tax, C. M. W., Grussu, F., Ianus, A., Bogusz, F., Pieciak, T., Ning, L., Larochelle, H., Descoteaux, M., Chamberland, M., Blumberg, S. B., Mertzanidou, T., Alexander, D. C., Afzali, M., Aja-Fernández, S., Jones, D. K., Westin, C.-F., ... Hutter, J. (2020). Acquiring and predicting multidimensional diffusion (MUDI) data: An open challenge. https://doi.org/10.1007/978-3-030-52893-517

Rajkowska, G., Selemon, L. D., & Goldman-Rakic, P. S. (1998). Neuronal and glial somal size in the prefrontal cortex. *Archives of General Psychiatry*, 55, 215–224. https://doi.org/10.1001/archpsyc.55.3.215

Reuter, M., Schmansky, N. J., Rosas, H. D., & Fischl, B. (2012). Within-subject template estimation for unbiased longitudinal image analysis. *NeuroImage*, 61, 1402–1418. https://doi.org/10.1016/j.neuroimage.2012.02.084

Reymbaut, A., Critchley, J., Durighel, G., Sprenger, T., Sughrue, M., Bryskhe, K., & Topgaard, D. (2021). Toward nonparametric diffusion-characterization of crossing fibers in the human brain. *Magnetic Resonance in Medicine*, 85, 2815–2827. https://doi.org/10.1002/mrm.28604

Rohde, G., Barnett, A., Basser, P., Marenco, S., & Pierpaoli, C. (2004). Comprehensive approach for correction of motion and distortion in diffusion-weighted MRI. *Magnetic Resonance in Medicine*, 51, 103–114. https://doi.org/10.1002/mrm.10677

Rubner, Y., Tomasi, C., & Guibas, L. (1998). *A metric for distributions with applications to image databases* (pp. 59–66). Narosa Publishing House. doi:10.1109/ICCV.1998.710701

Schilling, K. G., Blaber, J., Huo, Y., Newton, A., Hansen, C., Nath, V., Shafer, A. T., Williams, O., Resnick, S. M., Rogers, B.,

Anderson, A. W., & Landman, B. A. (2019). Synthesized b0 for diffusion distortion correction (Synb0-DisCo). *Magnetic Resonance Imaging*, 64, 62–70. https://doi.org/10.1016/j.mri.2019.05.008

Schilling, K. G., Fadnavis, S., Batson, J., Visagie, M., Combes, A. J., By, S., McKnight, C. D., Bagnato, F., Garyfallidis, E., Landman, B. A., Smith, S. A., & O'Grady, K. P. (2023). Denoising of diffusion MRI in the cervical spinal cord–Effects of denoising strategy and acquisition on intra-cord contrast, signal modeling, and feature conspicuity. *NeuroImage*, 266, 119826. https://doi.org/10.1016/j.neuroimage.2022.119826

Shemesh, N., Jespersen, S. N., Alexander, D. C., Cohen, Y., Drobnjak, I., Dyrby, T. B., Finsterbusch, J., Koch, M. A., Kuder, T., Laun, F., Lawrenz, M., Lundell, H., Mitra, P. P., Nilsson, M., Özarslan, E., Topgaard, D., & Westin, C. F. (2015). Conventions and nomenclature for double diffusion encoding NMR and MRI. *Magnetic Resonance in Medicine*, 75, 82–87. https://doi.org/10.1002/mrm.25901

Sjolund, J., Szczepankiewicz, F., Nilsson, M., Topgaard, D., Westin, C.-F., & Knutsson, H. (2015). Constrained optimization of gradient waveforms for generalized diffusion encoding. *Journal of Magnetic Resonance*, 261, 157–168. https://doi.org/10.1016/j.jmr.2015.10.012

Slator, P. J., Hutter, J., Palombo, M., Jackson, L. H., Ho, A., Panagiotaki, E., Chappell, L. C., Rutherford, M. A., Hajnal, J. V., & Alexander, D. C. (2019). Combined diffusion-relaxometry MRI to identify dysfunction in the human placenta. *Magnetic Resonance in Medicine*, 82, 95–106. https://doi.org/10.1002/mrm.27733

Slator, P. J., Palombo, M., Miller, K. L., Westin, C., Laun, F., Kim, D., Haldar, J. P., Benjamini, D., Lemberskiy, G., de Almeida Martins, J. P., & Hutter, J. (2021). Combined diffusionrelaxometry microstructure imaging: Current status and future prospects. *Magnetic Resonance in Medicine*, 86, 2987–3011. https://doi.org/10.1002/mrm.28963

Stanisz, G. J., & Henkelman, R. M. (1998). Diffusional anisotropy of T2 components in bovine optic nerve. *Magnetic Resonance in Medicine*, 40, 405–410.

Stejskal, E., & Tanner, J. (1965). Spin diffusion measurements: Spin echoes in the presence of a time-dependent field gradient. *Journal of Chemical Physics*, 42, 288–292.

Stepišnik, J. (1981). Analysis of NMR self-diffusion measurements by a density matrix calculation. *Physica B+C*, 104, 350–364. https://doi.org/10.1016/0378-4363(81)90182-0

Stepišnik, J. (1985). Measuring and imaging of flow by NMR. *Progress in Nuclear Magnetic Resonance Spectroscopy*, 17, 187–209. https://doi.org/10.1016/0079-6565(85)80008-X

Stepišnik, J. (1993). Time-dependent self-diffusion by NMR spin-echo. *Physica B: Condensed Matter*, 183, 343–350. https://doi.org/10.1016/0921-4526(93)90124-O

Topgaard, D. (2019). Diffusion tensor distribution imaging. *NMR in Biomedicine*, 32, e4066. https://doi.org/10.1002/nbm.4066

Veraart, J., Fieremans, E., & Novikov, D. S. (2016). Diffusion MRI noise mapping using random matrix theory. *Magnetic Resonance in Medicine*, 76, 1582–1593. https://doi.org/10.1002/mrm.26059

Veraart, J., Novikov, D. S., Christiaens, D., Ades-aron, B., Sijbers, J., & Fieremans, E. (2016). Denoising of diffusion MRI using random matrix theory. *NeuroImage*, 142, 394–406. https://doi.org/10.1016/j.neuroimage.2016.08.016

Veraart, J., Novikov, D. S., & Fieremans, E. (2018). Te dependent diffusion imaging (TEDDI) distinguishes between compartmental T2 relaxation times. *NeuroImage*, 182, 360–369. https://doi.org/10.1016/j.neuroimage.2017.09.030

Veraart, J., Raven, E. P., Edwards, L. J., Weiskopf, N., & Jones, D. K. (2021). The variability of mr axon radii estimates in the human white matter. *Human Brain Mapping*, 42, 2201–2213. https://doi.org/10.1002/hbm.25359

Wagner, F., Laun, F. B., Kuder, T. A., Mlynarska, A., Maier, F., Faust, J., Demberg, K., Lindemann, L., Rivkin, B., Nagel, A. M., Ladd, M. E., Maier-Hein, K., Bickelhaupt, S., & Bach, M. (2017). Temperature and concentration calibration of aqueous polyvinylpyrrolidone (PVP)

solutions for isotropic diffusion MRI phantoms. *PLoS One*, 12, e0179276. https://doi.org/10.1371/journal.pone.0179276

Wei, X., Zhu, L., Zeng, Y., Xue, K., Dai, Y., Xu, J., Liu, G., Liu, F., Xue, W., Wu, D., & Wu, G. (2022). Detection of prostate cancer using diffusion-relaxation correlation spectrum imaging with support vector machine model – A feasibility study. *Cancer Imaging*, 22, 77. https://doi.org/10.1186/s40644-022-00516-9

Weiskopf, N., Edwards, L. J., Helms, G., Mohammadi, S., & Kirilina, E. (2021). Quantitative magnetic resonance imaging of brain anatomy and in vivo histology. *Nature Reviews Physics*, 3, 570–588. https://doi.org/10.1038/s42254-021-00326-1

Westin, C.-F., Szczepankiewicz, F., Pasternak, O., Ozarslan, E., Topgaard, D., Knutsson, H., & Nilsson, M. (2014). Measurement tensors in diffusion MRI: Generalizing the concept of diffusion encoding. *Medical image computing and computer-assisted intervention*, 17(Pt 3), 209–216. https://doi.org/10.1007/978-3-319-10443-027

Wetscherek, A., Stieltjes, B., & Laun, F. B. (2015). Flow-compensated intra-voxel incoherent motion diffusion imaging. *Magnetic Resonance in Medicine*, 74, 410–419. https://doi.org/10.1002/mrm.25410

Whittall, K. P., & MacKay, A. L. (1989). Quantitative interpretation of NMR relaxation data. *Journal of Magnetic Resonance (1969)*, 84, 134–152. https://doi.org/10.1016/0022-2364(89)90011-5

Williamson, N. H., Ravin, R., Benjamini, D., Merkle, H., Falgairolle, M., O'Donovan, M. J., Blivis, D., Ide, D., Cai, T. X., Ghorashi, N. S., Bai, R., & Basser, P. J. (2019). Magnetic resonance measurements of cellular and sub-cellular membrane structures in live and fixed neural tissue. *eLife*, 8, e51101. https://doi.org/10.7554/eLife.51101

Woessner, D. E. (1963). NMR spin-echo self-diffusion measurements on fluids undergoing restricted diffusion. *The Journal of Physical Chemistry*, 67, 1365–1367. https://doi.org/10.1021/j100800a509

Xu, J., Li, H., Li, K., Harkins, K. D., Jiang, X., Xie, J., Kang, H., Dortch, R. D., Anderson, A. W., Does, M. D., & Gore, J. C. (2016). Fast and simplified mapping of mean axon diameter using temporal diffusion spectroscopy. *NMR in Biomedicine*, 29, 400–410. https://doi.org/10.1002/nbm.3484

Yon, M., de Almeida Martins, J. P., Bao, Q., Budde, M. D., Frydman, L., & Topgaard, D. (2020). Diffusion tensor distribution imaging of an in vivo mouse brain at ultrahigh magnetic field by spatiotemporal encoding. *NMR in Biomedicine*, 33, e4355. https://doi.org/10.1002/nbm.4355

Yon, M., Narvaez, O., Martin, J., Jiang, H., Bernin, D., Forssell-Aronsson, E., Laun, F., Sierra, A., & Topgaard, D. (2023). Frequency-dependence in multidimensional diffusion-relaxation correlation MRI of the brain: overfitting or meaningful parameter? *bioRxiv* https://doi.org/10.1101/2024.04.29.59158

Zhang, Z., Wu, H. H., Priester, A., Magyar, C., Afshari Mirak, S., Shakeri, S., Mohammadian Bajgiran, A., Hosseiny, M., Azadikhah, A., Sung, K., Reiter, R. E., Sisk, A. E., Raman, S., & Enzmann, D. R. (2020). Prostate microstructure in prostate cancer using 3-T MRI with diffusion-relaxation correlation Spectrum imaging: Validation with whole-mount digital histopathology. *Radiology*, 296(2), 348–355.

SUPPORTING INFORMATION

Additional supporting information can be found online in the Supporting Information section at the end of this article.